Grain Boundaries in Fe-Based Superconductors

Jens Hänisch and Kazumasa Iida

10.1 Introduction

The discovery of Fe-based superconductors (FBS) [1, 2] had a huge impact on the condensed matter community, since understanding the mechanism of superconductivity of this class of materials shed light on exploring new high-T_c superconductors. Therefore, a lot of effort has been devoted to unveiling physics of these compounds, resulting in several important findings: (a) five orbitals of Fe 3*d* cross the Fermi level (i.e. multiband superconductors) [3], (b) the symmetry of the superconducting order parameter (OP) is identified as $s_{\pm}$ wave (i.e. unconventional superconductor) both theoretically and experimentally (note: this may depend on the system and also doping level) [3–5], (c) the short coherence length results from the low Fermi velocity and small carrier concentration [6], and (d) the parent phase is an antiferromagnet. Although some of the features are similar to the cuprates, there are distinct differences between those two classes. For instance, (1) the symmetry of the OP for FBS is not a *d*-wave but an extended *s*-wave, (2) the parent compounds of FBS are not Mott insulators but semimetals [note: among the FBS only $A_{1-x}Fe_{2-y}As_2$ (A=K, Cs, Rb, Tl) is Mott insulator], (3) grain boundaries are of metallic nature, and (4) anisotropies of upper critical field (H_{c2}) and also critical current density (J_c) of FBS are smaller than those of the cuprates. Additionally, experiments on Co-doped $BaFe_2As_2$ (Ba122) bicrystal films revealed early on that exponential decay of J_c across the symmetric [001]-tilt grain boundary starts at a misorientation angle of 9° [7], which is almost twice as large as for the cuprates [8].

J. Hänisch (✉)
Institute for Technical Physics, Karlsruhe Institute of Technology, Eggenstein-Leopoldshafen, Germany
e-mail: jens.haenisch@kit.edu

K. Iida
Department of Materials Physics, Nagoya University, Chikusa, Nagoya, Japan
e-mail: iida@mp.pse.nagoya-u.ac.jp

Thanks to those features, J_c across grain boundaries in FBS is not severely reduced compared to the cuprates, which is favourable for wire as well as polycrystalline bulk applications.

To date, FBS wires and tapes have been fabricated by two methods: (1) the powder-in-tube (PIT) method for which precursor powders are put into metallic tube, swaged, drawn, and then heat-treated, and (2) the coated conductor method for which pseudo single crystalline films are deposited on technical metallic substrates. Hence, FBS wires and tapes contain grain boundaries.

Grain boundaries (GBs) as two-dimensional defects have huge influence on macroscopic properties of functional materials [9, 10] and are therefore of high interest in their development. They comprise the more or less planar structure between two adjacent crystallites of different crystallographic orientation. Grain boundaries are in general characterized by five parameters, i.e. the GB plane with respect to one of the crystallites (characterized by its normal vector **n** (two parameters), the rotation axis **u** (two parameters), and the GB angle θ_{GB}, for which the second crystallite is rotated around **u** away from orientation of crystallite 1), Fig. 10.1. In polycrystalline bulk samples, in general different types of GBs co-exist. In well-defined experiments on single GBs, however, usually special types of GBs are used and investigated, such as twist-boundaries (**u**||**n**), tilt-boundaries (**u**⊥**n**), symmetric boundaries (GB plane is mirroring the two crystallites), and low-Σ GBs (special GB angles for large coincidence lattices). A further classification may be done via the GB angle θ_{GB} [11]: Low-angle GBs (LAGBs) are comprised of an array of dislocations with distance $D = b/\{2\sin(2\theta_{GB})\} \sim b/\theta_{GB}$ (Frank's formula) in the simplest and most symmetric case, where b is the magnitude of the dislocation's Burgers vector **b** (usually a lattice constant) along the GB. At around 10–15°, depending on the material, the cores or distorted regions of adjacent dislocations start to get in contact to each other and it gets energetically favourable

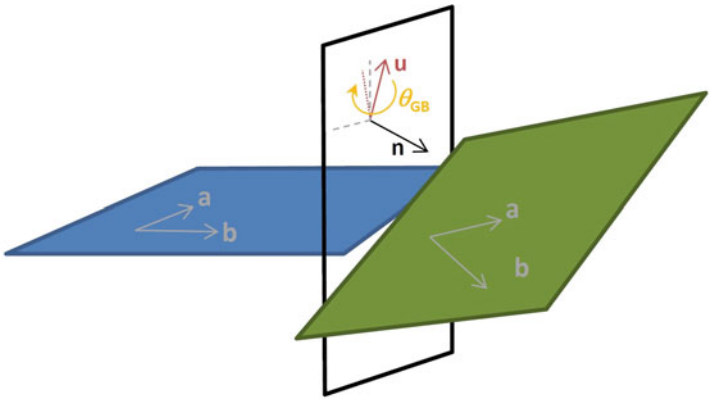

Fig. 10.1 Schematic of a grain boundary with grain boundary plane **n**, rotation axis **u**, and rotation angle θ_{GB}. The dashed lines represent the orthogonality of **n** on the GB plane, the dotted line is the projection of **u** on the GB plane

for the GB to reconstruct in bigger structural units. This is the angular regime of high-angle GBs (HAGBs).

In superconducting materials, GBs not only influence the structural and mechanical but also the electrical properties. In low-T_c superconductors, such as Nb_3Sn, GBs are known to be good flux pinning centres, so that an increase in GB density (or decrease in grain size) often leads to an increase of the critical current density J_c, e.g. [12]. In the high-T_c cuprates (HTS), however, GBs posed a huge obstacle for realizing high-current applications since high-angle GBs severely diminish the critical current densities J_c. In fact, above some critical angle θ_c, J_c falls exponentially with θ_{GB}, as has been measured for several cuprate compounds, such as $YBa_2Cu_3O_7$ (YBCO) [13] and $Bi_2Sr_2Ca_{n-1}Cu_nO_{2n+4}$ [14], see Fig. 10.2. For reviews on GBs in HTS bulks and films, see [8, 15]. There are several reasons for this strong $J_c(\theta_{GB})$ dependence: First of all, HTS are extreme type-II superconductors with very small coherence lengths ξ of only a few nm and very low charge carrier densities. This leads to depletion in Cooper pair density within the (high-angle) GB region which usually has a width comparable to or even larger than ξ, or around the dislocations of LAGBs due to e.g. stoichiometry deviations, band bending, charge inhomogeneities, and strain dependence of T_c. Therefore, HAGBs usually constitute weak links in HTS materials, and since the width of GBs approximately increases linearly with GB angle and tunnel currents fall exponentially with tunnel barrier width, an exponential decrease of J_c with GB angle θ_{GB} follows naturally. Depending on θ_{GB} and amount of faceting of the GB plane, J_c may be further diminished by possible destructive overlap of positive and negative regions of the wave function due to the d-wave symmetry in HTS [16]. Low-angle grain boundaries with sufficiently low θ_{GB} only minimally disturb the current flow, and their dislocations may even contribute to flux pinning [17].

In superconductors with low charge carrier concentrations, such as the HTS cuprates and to some part the Fe-based superconductors, there exists a further

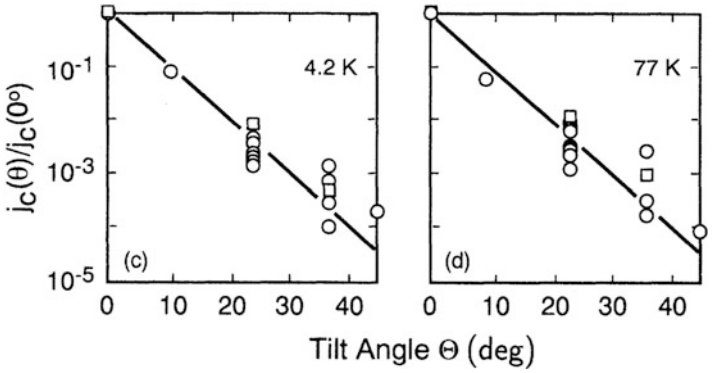

Fig. 10.2 Angle dependence of the reduced critical current density across [001]-tilt grain boundaries in YBCO (squares) and Bi2212 (circles) at 4.2 and 77 K. Reprinted figure with permission from [14]. Copyright (1995) by the American Physical Society

intermediate regime, where the electronically disturbed region around the dislocation cores is slightly larger than the structurally disturbed region. This has been discussed e.g. by a T_c reduction due to strain fields in cuprates. Therefore, in such GBs (with θ_{GB} slightly larger than the critical angle θ_c), the order parameter may be reduced along the entire GB plane and J_c would be reduced even though the GB is structurally still a LAGB. For GB angles slightly smaller than θ_c in contrast, the behaviour of the GB depends strongly on the applied magnetic field, since the magnetic field determines which kind of vortices are present within the GB plane—Abrikosov, Abrikosov-Josephson, or Josephson vortices.

In this chapter, GB issues of Fe-based superconductors will be discussed in more or less historical order on polycrystalline bulks and wires followed by bicrystal and polycrystalline thin films for the most-studied, application-relevant systems: *Ln*FeAs(O,F) (*Ln* lanthanoids), P-, Co-, and Ni-substituted AeFe$_2$As$_2$, (*Ae*: alkali earth) and Fe(Se,Te) in comparison to the cuprate high-T_c superconductors. Earlier reviews on GBs in FBS materials have been published by Deutscher [18] and Durrell et al. [19]. The topic of microelectronic junctions on bicrystal GBs in FBS has been reviewed, e.g. by Seidel [20], and is not covered here.

10.2 Grain Boundaries in Polycrystals and PIT Wires

Fe-based superconductors showed very high upper critical fields H_{c2} with low anisotropy despite anisotropic crystal structure. Hence, the community in applied superconductivity research has imagined this material class to have potential for conductor or bulk applications in high fields. And the question arose immediately which (critical) current can be circulated in polycrystalline bulk samples or transported in powder-in-tube (PIT) wires of Fe-based superconductors. To address this issue, many studies have been conducted on such polycrystalline samples. In this subsection, these studies on polycrystalline *Ln*FeAsO, LiFeAs, AeFe$_2$As$_2$, and Fe chalcogenides will be introduced.

10.2.1 LnFeAsO (Ln: Lanthanoids) Sintered Bulks

Sintered SmFeAsO$_{1-\delta}$ and NdFeAs(O,F) bulk samples have been well characterized immediately after the discovery of FBS. Unlike AeFe$_2$As$_2$ (*Ae*122) and FeSe systems, sizable single crystals of *Ln*1111 were difficult to grow in the early stages of FBS research. Therefore, the electromagnetic properties of *Ln*1111 were characterized using polycrystalline samples. Figure 10.3 shows the microstructure of polycrystalline SmFeAsO$_{0.85}$ acquired by a scanning electron microscope [21]. Clearly, some of the plate-like SmFeAsO$_{0.85}$ grains were well connected (i.e. clean grain boundary without cracks). On the other hand, cracks between the SmFeAsO$_{0.85}$ grains as well as occasionally within grains (Fig. 10.4a) were

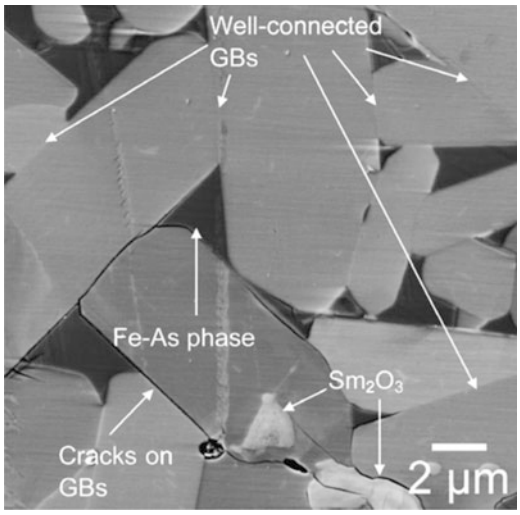

Fig. 10.3 SEM image of partially well-connected Sm1111 grains. Current transport is obstructed by FeAs, Sm_2O_3 and cracks at the grain boundaries. Republished with permission of IoP Publishing, from [21]; permission conveyed through Copyright Clearance Center, Inc.

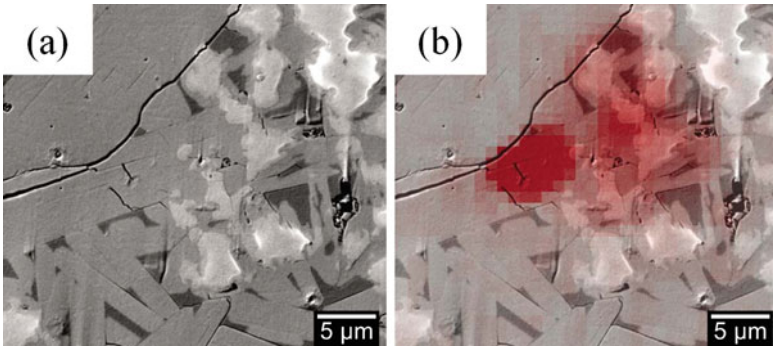

Fig. 10.4 Higher resolution SEM image (**a**) near a dissipation spot (red, **b**) in a $SmFeAsO_{0.85}$ polycrystal determined by low-temperature laser scanning microscopy (LTLSM). Current transport is obstructed by FeAs, Sm_2O_3, and cracks. Reprinted from [22], with permission of AIP Publishing

frequently observed, which impedes the critical current flow within the grains. Also Sm_2O_3 as well as FeAs were observed around the $SmFeAsO_{0.85}$ grains, which act as global current blockers (i.e. the overall critical current flowing through a sample via adjacent grains is reduced). Indeed, strong dissipation spots were observed near such defects because the current is squeezed into narrow paths without current blockers (Fig. 10.4a, b) [22].

The derivatives of the field dependence of remnant magnetization (m_R) for the $SmFeAsO_{0.85}$ bulk sample revealed two distinct peaks (Fig. 10.5): the former reflects the global J_c (J_c^{global}) and the latter corresponds to the intra-grain one (J_c^{local} or J_c^{Grain}) [23]. The respective global and intra-grain J_c at 5 K were 3900 A/cm^2 and 4.5 $\times$ 10^6 A/cm^2, indicating that SmFeAsO inherently possesses high J_c. Hence, eliminating such extrinsic defects like wetting FeAs and cracks would lead

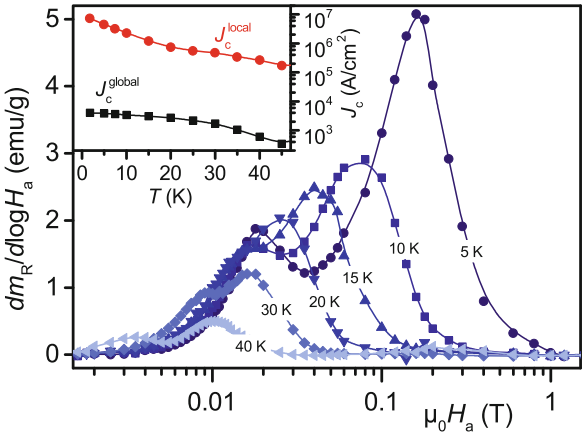

Fig. 10.5 Derivatives of the remanent magnetization as a function of the maximum applied field for the $SmFeAsO_{0.85}$ small bulk [23]. Data are normalized by sample mass. Inset shows the temperature dependences of the peak fields $\mu_0 H_{peak}$ for the first and second peaks. Data courtesy of A. Yamamoto

to high J_c^{global}. It is worth mentioning that J_c^{global} of $SmFeAsO_{0.85}$ is much higher than that of sintered $YBa_2Cu_3O_7$ in early days ($\sim$100 A/cm^2 at 4 K) [24]. The temperature dependence of J_c^{global} at low-temperature regime is well described by $J_c^{global} \sim (T_c - T)^2$, which indicates that J_c^{global} is governed by an SNS (S: superconductor and N: normal metal) proximity coupled Josephson junction network [23]. Indeed, J_c^{global} is significantly reduced by a small magnetic field. In later $SmFeAsO_{0.85}$ samples, a J_c^{global} of only $\sim$250 A/cm^2 was measured despite much better phase purity and grain connectivity achieved by hot-isostatic pressing [25]. This was partially attributed to lower T_c values and a possibly different F content and distribution. Similar results of J_c^{global} $\sim$100–200 A/cm^2 were measured by Eisterer et al. [26] and Otabe et al. [27] on $SmFeAsO_{1-x}F_x$ bulk samples.

So far, we discussed only the effect of extrinsic factors on the inter-grain J_c. To understand the intrinsic effect, bicrystal experiments on well-defined, single grain boundaries should be necessary. Unlike *Ae*122 and FeSe systems, such experiments have not been reported until 2018. Very recently, misorientation angle dependence of the inter-grain J_c for NdFeAs(O,F) bicrystal films has been reported [28, 29], which will be discussed in Sect. 10.3.1.

Despite the absence of bicrystal experiments on *Ln*1111, several pieces of important information necessary to achieve high global J_c values were revealed by the studies mentioned above (i.e. reducing the amount of impurity phases like FeAs and Ln_2O_3, increasing the sample density and texturing to improve grain connectivity, and reducing the number of cracks within grains). Hence, a lot of activities for fabricating *Ln*1111 wires and tapes have kept going, resulting in the improvement of J_c performance step by step over time [30–33]. Here, the wire fabrication focuses on SmFeAs(O,F) because of the highest T_c among the FBS in the bulk form. One breakthrough for achieving high global J_c values in polycrystalline SmFeAs(O,F) wires was to add Sn to the precursor powders, which reduces the amount of FeAs wetting at grain boundaries due to the chemical reaction between FeAs and Sn producing $FeSn_2$ particles or discontinuous layers (Fig. 10.6) [30].

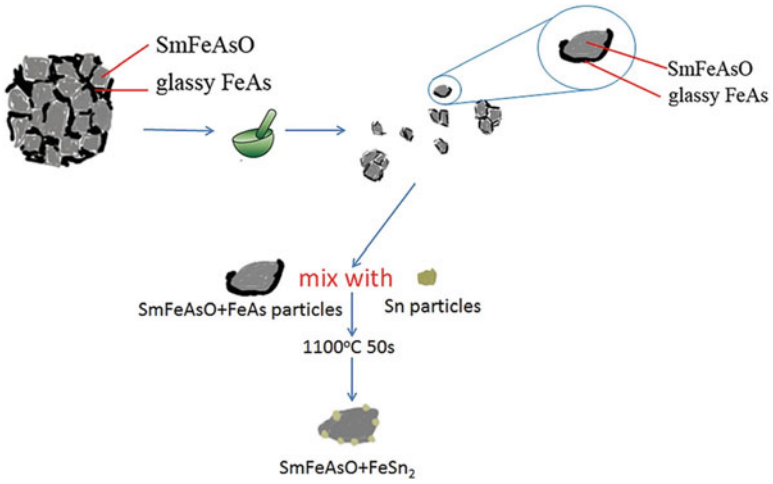

Fig. 10.6 Schematic diagram describing the Sn transformation which eliminates the detrimental FeAs wetting phase but also damages $SmFeAsO_{1-x}F_x$ grains, i.e. reduces T_c. Reprinted from [30], with permission of AIP Publishing

Sn addition, however, leads to a slight decrease in T_c (T_{c0} decreased from 43.3 to 37 K). Another effect of Sn addition is filling voids and cracks, which improves the grain connectivity. Adding metallic elements such as Ag, Pb, and Sn have been reported in *Ae*122 for improving grain connectivity and hence, superconducting properties [34–36]. At present, the self-field J_c of SmFeAs(O,F) wires was achieved around 4×10^4 A/cm^2 at 5 K [37]. Although the significant improvement of wire performance of *Ln*1111 has been achieved since 2008, self-field as well as in-field J_c are still one or two order of magnitude lower than *Ae*122. One of the challenging issues for SmFeAs(O,F) wires is to control the F content. Employing low synthesis temperatures guarantees a high T_c of over 50 K, however, the presence of unreacted phase and low sample density still remain. Further optimization of the SmFeAs(O,F) wire fabrication is necessary.

10.2.2 $AeFe_2As_2$ (Ae: Alkali Earth Elements) Sintered Bulks

Although the maximum T_c of *Ae*122 is close to that of MgB_2 [between Fe(Se,Te) and SmFeAs(O,F)], the activity of wires and bulk fabrications using *Ae*122 is quite high thanks to the highest depairing current density among the FBS. For bulk and wire fabrications, high-energy ball-milling has been employed to synthesis *Ae*122 precursor powders [34–36, 38, 39]. During the ball-milling, partial Ba122 phase formation occurs. The resultant precursor powders are highly homogeneous and reactive. Hence, it is possible to reduce the heat treatment temperature, resulting in

the absence of GB wetting phases. The combination of fine precursor powders with highly phase-pure and high-pressure synthesis (i.e. cold and hot isostatic pressing) yields over 90% relative density in K-substituted Ba122 [38]. As a result, transport critical current densities of untextured bulks and round wires of K-doped Ba122 exceed 10^5 A/cm^2 in self-field at 4.2 K. Similarly, Co-doped Ba122 fabricated by the same method showed a self-field J_c of over 2×10^4 A/cm^2 at 4.2 K. These results highlight the application potential of FBS wires and bulk magnets.

The microstructures of a K-doped Ba122 sample prepared with high-energy ball-milling are shown in Fig. 10.7 [38]. As stated earlier, the grain boundaries are notably clean without FeAs wetting phase, which was frequently observed in *Ln*FeAs(O,F).

The detailed analyses by atom probe tomography (APT) revealed a trace of oxygen impurities along the GBs (see Fig. 10.8) [40], which is consistent with the results for K-doped Sr122 reported by Wang et al. [41]. It is still unclear whether the GB oxides are due to impurities of the precursor material or form during (bulk) sample preparation. A formation during APT sample preparation is less likely (the outer surfaces do not contain oxygen), however cannot be excluded completely. To understand whether this is an extrinsic effect, further experiments should be carried out.

Although K-doped Ba- and Sr122 bulks and wires contain high-angle GBs, their global J_c is in the order of $10^4 \sim 10^5$ A/cm^2 at 4.2 K with and without magnetic fields. Additionally, recent experiments on K-doped Ba122 bulk samples with 10 mm in diameter and 18 mm thickness (in total) revealed a large trapped magnetic field of over 1 T at 5 K [42]. Nevertheless, even though the microstructures are very similar, the J_c performance of Co-doped Ba122 is inferior to that of K-doped Ba122 by almost one order of magnitude [38]. This indicates that grain boundary properties depend on the kind of substituting elements (i.e., K, Co, and P) and perhaps *Ae* in *Ae*Fe_2As_2 too, by extrinsic and/or intrinsic effects. To clarify this, bicrystal experiments on (Ba,K)Fe_2As_2 and (Sr,K)Fe_2As_2, which are still missing, are desirable.

It is reported that the inter-grain J_c of Co-doped Ba122 bicrystal films decays exponentially beyond a misorientation angle (θ_{GB}) of 9° [7]. However, the inter-grain J_c is almost constant $10^4 \sim 10^5$ A/cm^2 above $\theta_{GB} = 30°$, which differs from the cuprates [8]. This level of J_c is consistent with the global J_c observed in polycrystalline K-doped Ba- and Sr122. Although bicrystal experiments on K-doped Ba- and Sr122 are absent, the same observations are highly likely. This similarity between bulk J_c^{global} and HAGBs in bicrystal films has two possible reasons: (1) Clean GBs may suffer from vortex channelling, which is larger in straight GBs such as in bicrystal films, (2) LAGBs in bulks may still contain oxides which let them appear as HAGBs by increasing the effective width. Hence, to further improve the global J_c for K-doped Ba- and Sr122, a texturing process might be useful. Indeed, textured 100 m long K-doped Sr122 tapes with an average large J_c of 10^4 A/cm^2 even at 10 T at 4.2 K have already been realized [43]. Besides texturing, clean oxide-free GBs in dense and crack-free materials are key for high J_c^{global} values.

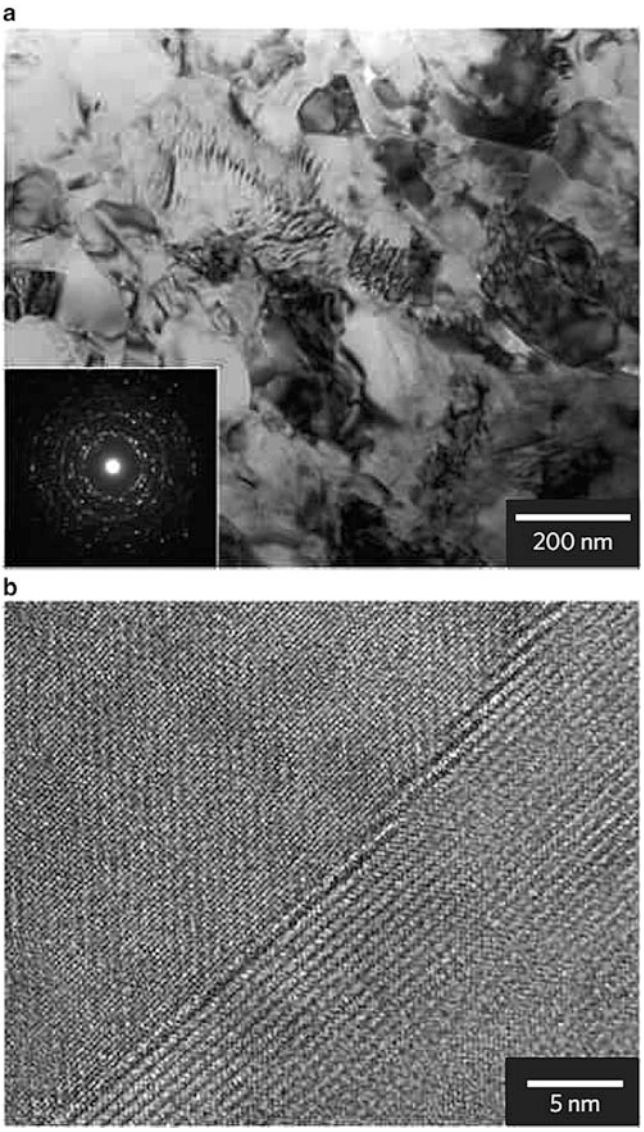

Fig. 10.7 Microstructure of K-doped Ba122 bulk investigated by TEM. (**a**) TEM image of polycrystalline K-doped Ba122 bulk material showing several equi-axed grains with average grain diameter of ∼200 nm. Inset: A selected-area electron diffraction image of (**a**) indicating that the grains of the material are randomly oriented with many high-angle GBs. (**b**) HRTEM image of a typical K-doped Ba122 GB. The lattice fringes of upper and bottom grains meet at the GB without an amorphous contrast, indicating that the GB is clean without a wetting impurity phase. Reprinted by permission from: Springer Nature, Nature Materials [38], Copyright (2012)

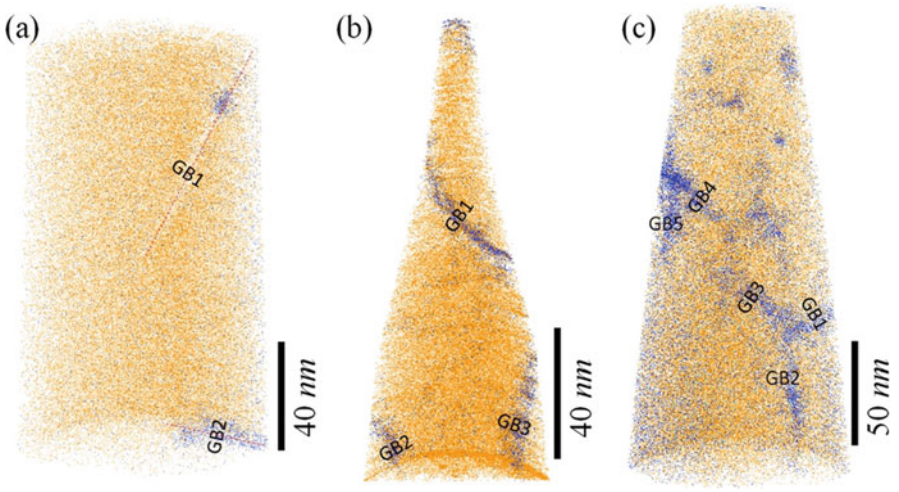

Fig. 10.8 A 3D atom probe tomographic reconstruction of: (**a**) $(Ba_{0.6}K_{0.4})Fe_2As_2$; (**b**) $(Ba_{0.4}K_{0.6})Fe_2As_2$; and (**c**) $Ba(Fe_{0.92}Co_{0.08})_2As_2$ superconductors. Oxygen atoms are in blue and Ba atoms are in orange, other elements are excluded for a clear display of grain boundary segregation. Each dot represents a single atom, but not to scale. Reprinted from [40], with permission of AIP Publishing

10.2.3 FeSe and Fe(Se,Te) Sintered Bulks

Most of the studies on *11* bulk samples focused on PIT-processed wires using FeSe and Fe(Se,Te) [45–48]. The strategy for achieving high transport J_c is the same as for other systems (i.e. eliminating extrinsic factors mentioned above together with texturing process). To realize the dense materials, Ding et al. reported a novel method to fabricate FeSe tapes [44]. In their method, an Fe sheet, $\sim 50 \times 5$ mm^2 in size, and Se grains were sealed together in an evacuated quartz tube and thermally treated. During the heat treatment, Se vapour reacted with Fe, resulting in the formation of FeSe. The microstructure of the resultant FeSe contained many grains with ~ 20 μm diameter (Fig. 10.9). Many cracks between grains were also observed. Although the self-field intra-grain J_c is as high as 10^4 A/cm^2 at 5 K, the inter-grain J_c at 4.2 K is 600 A/cm^2.

One of the breakthroughs for improving the global J_c for Fe(Se,Te) is a novel process in which the precursor materials are melted, followed by annealing [49]. Figure 10.10 compares the microstructures of Fe(Se,Te) bulk samples after different preparations. As can be seen, a lot of pores were observed in the Fe(Se,Te) sintered sample with a grain size almost comparable to the pores. On the other hand, the melt-processed sample showed less porosity. Additionally, no secondary phases were observed at GBs. Annealing of that sample leads to stronger phase separation of regions with high and low Se-Te ratio as well as to formation of fine Fe-deficient precipitates (M+A). The resultant self-field J_c at 4.2 K is in the range of

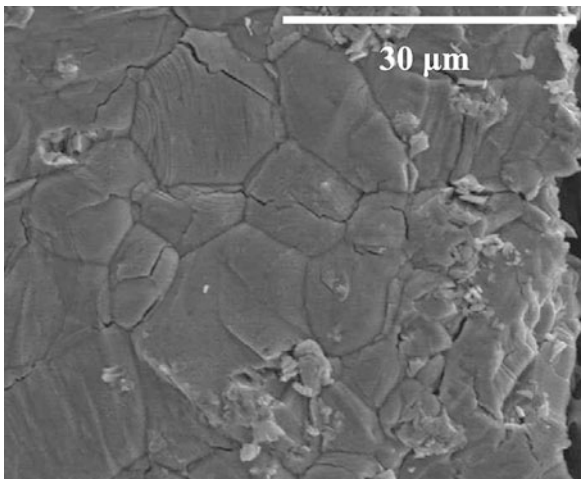

Fig. 10.9 SEM image of an FeSe tape. Republished with permission of IoP Publishing, from [44]; permission conveyed through Copyright Clearance Center, Inc.

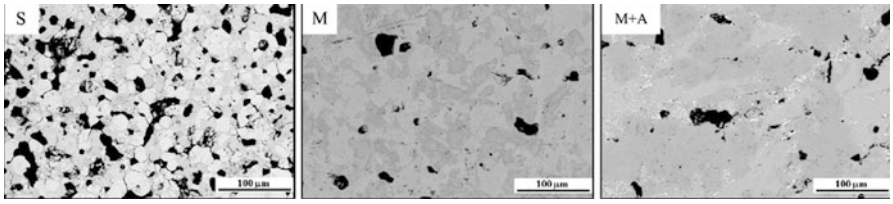

Fig. 10.10 Back-scattered SEM images of three polycrystalline Fe(Se,Te) samples. **S** sintered, **M** melted, **M**+**A** melted + annealed sample (at 550 °C, 17 days). Republished with permission of IoP Publishing, from [49]; permission conveyed through Copyright Clearance Center, Inc.

1000 A/cm^2, where the in-field J_c is almost constant up to 8 T. The level of J_c is two orders of magnitude lower than that of K-doped *Ae*122. The bicrystal experiments on Fe(Se,Te) showed the level of J_c at 4.2 K is between 10^3 and 10^4 A/cm^2 above $\theta_{GB} = 24°$ [50], which is comparable to that of the melt-processed/annealed Fe(Se,Te) with dense microstructure and clean GBs. Hence it may be concluded, texturing is necessary for further improvement of J_c, which is similar to the *Ae*122 systems.

Mancusi et al. [51] used an $FeSe_{0.5}Te_{0.5}$ polycrystalline bulk sample to study the effect of GB networks on the complex AC susceptibility response $\chi(T)$ near T_c. The transition shows clear two-step behaviour, especially for the imaginary part χ'', for all AC fields and frequencies tested, which were fitted by taking into account the actual induced fields and relaxation times in the GB region and within the grains. Flux motion in both regions was found to be flux creep at low T and thermally activated flux flow (TAFF) at high T. T_c of the GB region with ∼12 K was found to be considerably lower than the intra-grain value of ∼14 K.

10.2.4 Sintered Bulks of LiFeAs and Other Compounds

The only GB study on *111* compounds has been conducted by Singh et al. [52] on LiFeAs polycrystalline bulk samples. This compound exhibits superconductivity ($T_c \sim 19$ K) without any doping. The samples were prepared by a solid-state reaction with a low-temperature of 600 °C. Although the precursor powder was uniaxially pressed into a pellet, followed by a low-temperature sintering, the sample had a relative density of 70%. Microstructural analysis revealed micro-cracks between the grains. Such micro-cracks may be formed due to the thermal stress. Another distinct feature is that the phase-pure LiFeAs sintered sample is chemically homogeneous. Therefore, micro-cracks are major current blockers, leading to a small inter-grain J_c of only ~440 A/cm^2 even at 5 K. As possible routes for future increase in inter-grain J_c, reducing the micro-crack density by process optimization, increasing the density by hot-isostatic pressing and texturing are suggested by Singh et al.

Also Fe-based superconductors with large blocking layers, $(Fe_2As_2)(Ca_4(Mg_{0.25}, Ti_{0.75})_3O_8)$ (22438, $T_c = 43$ K) and $(Fe_2As_2)(Ca_5(Sc_{0.5}Ti_{0.5})_4O_{11})$ (225411, $T_c = 36$ K) have been investigated regarding their GBs [53]. Both compounds showed weak-link behaviour with the typical two-step transition in remanent magnetization vs. applied field, where 22438 shows slightly better grain connectivity due to cleaner GBs. The inter-grain J_c values around 0.5 and 0.07 MA/cm^2 are relatively low compared to other FBS bulks of similar T_c. Both samples show a double transition in the in-field temperature dependence of the resistivity which also has been attributed to electromagnetic granularity. However, since for the cuprates polycrystalline samples usually show a double transition also in self-field [54] and $Bi_2Sr_2Ca_{n-1}Cu_nO_{2n+4}$ single crystals show similar in-field behaviour [55], this behaviour as well as the low J_c values might also be attributable to the extremely large electronic anisotropy in these compounds.

Recently, magnetization J_c values of a $CaKFe_4As_4$ (1144) single crystal have been compared to a pressed powder sample made from such a single crystal [56]. Whereas the single crystal shows exceptionally high J_c values (up to 200 MA/cm^2 for $B \perp c$ and 10 MA/cm^2 for $B||c$[1]), the powder exhibits much reduced J_c values (~40 kA/cm^2) due to weak-link behaviour at the GBs. However, this is still larger than for other FBS bulks.

10.2.5 Summary

Also for FBS, high-angle GBs suppress the super-current flow due to the deterioration of the superconducting OP at GBs. Although the origins of the deterioration of the superconducting OP at GBs for the cuprates [46, 57] have been identified

[1]Due to the complex microstructure of these samples with different kinds of stacking faults and intergrowths, the magnetically measured self-field J_c values differ for $\boldsymbol{B}||\boldsymbol{c}$ and $\boldsymbol{B} \perp \boldsymbol{c}$.

[8], it is still ambiguous for FBS. Further investigations using bicrystal films are necessary to understand GB characteristics, which will help to tackle GB issues. What can be said, however, is that in bulk samples GBs are affected severely by extrinsic properties, such as compactness and cleanliness. As shown in Table 10.1, $J_c{}^{global}$ is around three orders of magnitude lower than $J_c{}^{local}$, almost irrespective of the compound. This is a much larger reduction than observed for LAGB bicrystal junctions (typically 1–1.5 orders of magnitude), see below. Therefore, extrinsic effects must play a role in polycrystalline bulk samples.

Hecher et al. [60] pointed out that small grains might be one key to high-field applications of untextured polycrystalline FBS samples. The authors modelled the hysteresis of J_c for increasing and decreasing fields (which is due to the irreversible intra-grain currents) and found excellent agreement to detailed SQUID and scanning Hall probe microscopy (SHPM) measurements. As the authors concluded, the maximum magnetic field B_{max} at which a polycrystalline wire is still reasonably applicable for a certain application current density $J_c{}^{app}$ is inversely proportional to the mode of the grain size distribution s_0 (i.e. the grain size s, where the probability density is maximum) and the thickness of the GB region d:

$$B_{max} \approx \frac{\phi_0}{2\pi^2} \frac{|J_0|}{J_c^{app}} \frac{1}{s_0 d}$$

where J_0 is the maximum Josephson current across a single GB.

Eisterer very recently proposed a mean-field percolation model for the J_c limitation in polycrystalline Fe-based superconductors [61]. Inputs of the model are the statistical abundance of GB angles for a given texture quality characterized by the in-plane and out-of-plane texture spreads ϕ_t and θ_t, and the GB angle dependence of J_c, which is assumed to be independent of the type of GB. Two

Table 10.1 Critical temperature T_c (transport or magnetization) as well as global ($\sim J_c{}^{GB}$) and local J_c ($\sim J_c{}^{Grain}$) for several Fe-based superconducting polycrystalline bulk samples at 5 K (except Fe(Se,Te) 4.2 K)

	Transp. T_c (K)	Magn. T_c (K)	Global J_c (kA/cm^2)	Local J_c (MA/cm^2)	References
Fe(Se,Te)	15.5		5.5	1.0	[49]
$SmFeAsO_{0.85}$	51		4.0	6.8	[23]
$NdFeAsO_{0.94}F_{0.06}$	44		2.0	4.2	[23]
LiFeAs	19.2		0.44	N.A.	[52]
$Ba(Fe,Co)_2As_2$	25		6.0	N.A.	[39]
$(Sr,K)Fe_2As_2$ w Ag		34	1.0	9.0	[58]
$(Sr,K)Fe_2As_2$ w/o Ag		34	N.A.	40	[58]
$(Ba,K)Fe_2As_2$		37.4	10	N.A.	[59]
$CaKFe_4As_4$		35 K	40	10 (B||c)	[56]
$(Fe_2As_2)(Ca_4(Mg_{0.25},Ti_{0.75})_3O_8)$		43	0.5	N.A.	[53]
$(Fe_2As_2)(Ca_5(Sc_{0.5}Ti_{0.5})_4O_{11})$		36	0.07	N.A.	[53]

special cases are discussed: Equal texture spreads ($\phi_t = \theta_t$) which leads to roughly exponential decrease of J_c with θ_t similar to the single-GB dependence $J_c(\theta_{GB})$, and random in-plane orientation ($\phi_t = \infty$) which leads to a decrease in J_c to 9% for perfect fibre texture ($\theta_t = 0°$) in the case of FBS and a slight decrease with θ_t. Considering the simple assumptions, the agreement to experimental data (shown for $Bi_2Sr_2Ca_{n-1}Cu_nO_{2n+4}$) is remarkable. Fully random textures cannot be modelled yet due to the lack of reliable information on HAGBs.

10.3 Single Grain Boundaries in Thin Films

There are in general two main reasons for investigating single GBs in superconducting films, mostly on bicrystal substrates having a single well-defined grain boundary: (1) to realize Josephson junctions with two superconducting electrodes for fundamental research and assessing their potential for electronics applications (usually on HAGBs), and (2) to check the J_c transparency of the GBs of several angles and hence determine $J_c(\theta_{GB})$, which is important information for wire applications (usually on rather LAGBs). The former has been reviewed in [20, 62] and is not covered here. To date, all bicrystal experiments on FBS have been conducted on symmetric [001]-tilt bicrystal substrates ($SrTiO_3$, MgO, and $(LaAlO_3)_{0.3}(Sr_2TaAlO_6)_{0.7}$ [LSAT]). To obtain deeper knowledge of GB characteristics of FBS, grain boundary experiments using different types of bicrystals (i.e. valley or roof-top [010]-tilt, [100]-twist, and asymmetric grain boundaries) would be necessary, since in general, the inter-grain J_c depends on the GB type, as shown for $YBa_2Cu_3O_7$ deposited on various types of bicrystals [63]. Different results are expected in case of different order parameter symmetry (e.g. *s*-wave or *d*-wave) as well as strain sensitivity and charge carrier density. In the following, results on [001]-tilt GBs in FBS bicrystal films will be summarized and discussed. Furthermore, J_c is also influenced strongly by the local geometry of the GB since GBs often do not follow their macroscopic GB plane but may be facetted or meander. By faceting of GBs, usually observed in bicrystal films with 3D grain growth mode [64], the energy of the GB and its effective width can be reduced due to the formation of small segments of low-Σ GBs. Meandering of GBs occurs in films with lamellar growth mode such as $YBa_2Cu_3O_7$ grown by chemical solution deposition [65]. Both types of GB microstructures have a positive effect on J_c due to decreased flux channelling along the macroscopic grain boundary plane and therefore better flux pinning, as well as due to possibly decreased GB widths for facetted GBs. To date, no studies of these effects on FBS films have been reported though.

10.3.1 LnFeAsO (Ln: Lanthanoids) Bicrystal Experiments

To date, regarding the *1111* structure only NdFeAs(O,F) bicrystal films have been investigated. A first experiment [28] was conducted on films prepared by a two-step process [66]: The parent compound NdFeAsO was deposited at 800 °C, and subsequently a NdOF over-layer was deposited at the same temperature. During the NdOF over-layer deposition, F diffuses into NdFeAsO, resulting in the F doping. The inter-grain J_c of these films was reduced by 30% even at $\theta_{GB} = 6°$, suggesting that the critical angle might be less than 6°. Microstructural analyses revealed that NdFeAs(O,F) and the MgO substrates were eroded by the fluorine, which diffuses preferentially along the GB. Hence, the obtained results were of extrinsic nature. To reveal the intrinsic GB characteristics of NdFeAs(O,F), excess F should be prevented. Later, the deposition temperature of NdOF was reduced to minimize this damage [29]. Figure 10.11 shows the misorientation dependence of the inter-grain J_c for these improved NdFeAs(O,F) films on [001]-tilt symmetric MgO bicrystal substrate. As a result, θ_c of NdFeAs(O,F) was found to be around 9°, which is almost the same angle as for Co-doped Ba122 and Fe(Se,Te). Although the deposition temperature of NdOF was reduced from 800 to 700 °C, the GB region for $\theta_{GB} = 24°$ was damaged, resulting in zero inter-grain J_c. Even for

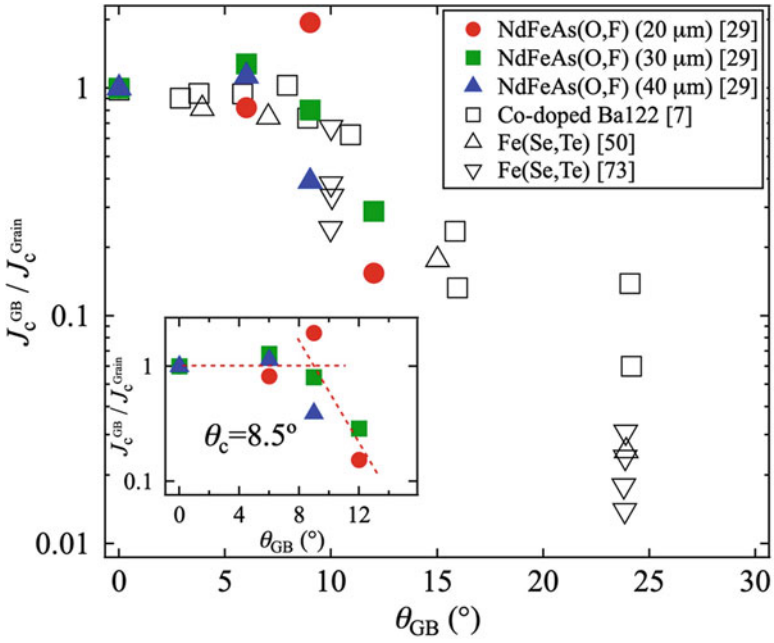

Fig. 10.11 Angle dependence of the reduced intra-grain critical current density (J_c^{GB}/J_c^{Grain}) for NdFeAs(O,F) bicrystal junctions (full symbols) measured using different bridge widths in comparison to $Ba(Fe,Co)_2As_2$ and Fe(Se,Te)

$\theta_{GB} = 6°$ the GB region was partially compromised by F. It is not ruled out that the damage to GB region by F had influenced the obtained results. To address these issues and to further explore the intrinsic GB characteristics, F-free *Ln*1111 like $Nd(Fe_{1-x}Co_x)AsO$ would be interesting although T_c is around 25 K.

10.3.2 $AeFe_2As_2$ (Ae: Alkali Earths) Bicrystal Experiments

Already in 2009, Lee et al. reported on the weak-link behaviour of [001]-tilt GBs in Co-doped Ba122 [67]. They deposited 350 nm thick films on $SrTiO_3$ bicrystals with angles θ_{GB} of 3°, 6°, 9°, and 24° by pulsed laser deposition (PLD). In low-temperature laser scanning microscopy (LTLSM) and magneto-optical imaging (MOI) on these Co-doped Ba-122 bicrystal junctions, the weak-link behaviour was revealed even for low-angle GBs (6° and 9°). These results suggested a critical angle θ_c below 6°, which differs from the results reported 2 years later by Katase, Hiramatsu et al. [7, 68], who estimated the critical angle to be around 9° from their bicrystal experiments on Co-doped Ba122 on MgO ($T_c = 20.7$ K) and LSAT (21.6 K). We speculate that increased oxygen diffusion from the $SrTiO_3$ substrate in the GB region led to a slightly larger disturbed region compared to other substrates (MgO, LSAT) which may have limited the LAGB J_c of Lee's films. However, the higher magnetic field (0.5 T) and temperatures (12–16 K) used by Lee et al. have to be taken into account (*n.b.* data at 12 K/0.5 T and 14 K/0 T, respectively, i.e. at low T and B are comparable to data by Katase et al., Fig. 10.12). However, T_c was only minimally reduced across the 6° junction on $SrTiO_3$ (20.3 vs. 20.5 K) and the resistive transitions were sharp and clean. We investigated HAGBs in Co-doped Ba122 films on Fe/spinel/$SrTiO_3$-bicrystal templates [69]. The critical angle was estimated to 8°; however, the normalized J_c of the HAGBs was one order of

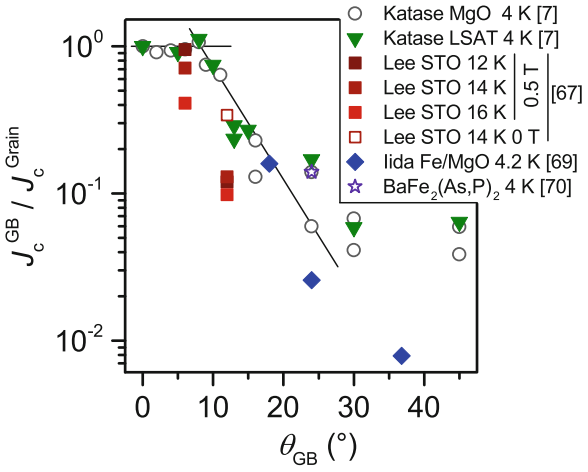

Fig. 10.12 GB angle dependence of the reduced intra-grain critical current density for $BaFe_2As_2$ bicrystal junctions

magnitude lower than reported by Katase et al., which again might be attributable to defects within the GB due to the oxygen diffusion from the $SrTiO_3$ substrate.

For MBE-grown P-doped Ba122 on MgO bicrystal, an even higher inter-grain J_c of >1 MA/cm^2 at 4 K for $\theta_{GB} = 24°$ was reported by Sakagami et al. [70], which can be attributed to the higher T_c (29.5 K) and intra-grain J_c compared to Co-doped Ba122. Although the number of data points is insufficient for a definite conclusion, P-doped Ba122 most likely also has a higher critical angle than the cuprates.

The GB angle dependence of J_c for GBs in $BaFe_2As_2$ is summarized in Fig. 10.12. Clearly, J_c remains equal to the intra-grain value up to $\theta_{GB} \sim 9°$. Beyond this angle, the exponential decay of the inter-grain J_c sets in. Furthermore, J_c^{GB} is nearly constant for 30° and 45°.

In single HAGBs, pinning effects can be observed occasionally, even though overall J_c might not be increased compared to the intra-grain values. An example is the 24° GB junction of $Ba(Fe,Co)_2As_2$ on $SrTiO_3$ in [67]. Although J_c is decreased in all magnetic fields, it shows a peak effect around 5–6 T which is attributable to pinning of Abrikosov-Josephson vortices at defects in the GB and by Abrikosov vortices in the adjacent grains. On MgO bicrystals [7], this effect might be recognizable although not discussed by the authors. In contrast, for the 37° GB on Fe/MgO [69] with strongly reduced J_c it was not observed. HAGBs may also indirectly contribute to flux pinning. Nanometric Fe particles tend to grow in or near 45° GBs, as observed in [71], which is due to the increased diffusion rates in GBs and/or strain effects. Compared to a similar sample without 45° misorientations, J_c was overall increased at all fields and field directions θ at medium temperatures (due to the slightly higher T_c value) and $J_c(\theta)$ showed a pronounced *c*-axis peak which was attributed to both the GBs and the Fe particles which were slightly elongated in *c*-direction.

10.3.3 Fe(Se,Te) Bicrystal Experiments

The self-field inter-grain J_c at 4.2 K of Fe(Se,Te) across a 45° grain boundary was measured by Sarnelli et al. to be around 10^4 A/cm^2, only one order of magnitude lower than the intra-grain J_c [73] (compared to four orders of magnitude for the cuprates). These results suggested that the J_c decrease with GB angle may not be as strong. Furthermore, J_c was more or less independent of bridge width and the Josephson current uniform across the junction width, which was explained by the *s*-wave symmetry in contrast to *d*-wave in cuprates. Later, these studies were completed by measuring the full $J_c(\theta_{GB})$ dependence by Si et al. [50] and Sarnelli et al. [72] where both groups came to similar and complementary results as shown in Fig. 10.13: Si et al. found that J_c^{GB} maintained $\sim 10^5$ A/cm^2 at 4.2 K for 4° and 7° also in relatively large applied magnetic fields of ~10 T, indicative of strong links. For $\theta_{GB} > 15°$, J_c^{GB} was significantly suppressed already by a small magnetic field and showed a foot structure in the temperature dependence of the resistivity, $\rho(T)$, which has been attributed to an increased disturbed region. It would be worth

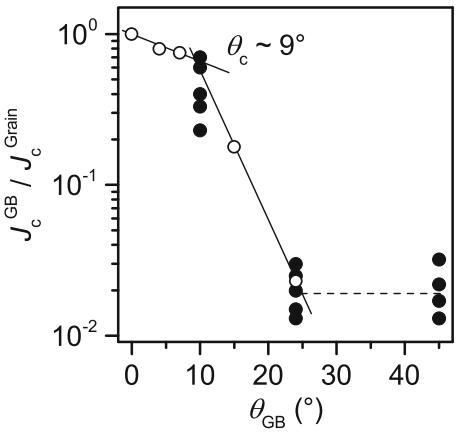

Fig. 10.13 Angle dependence of the reduced intra-grain critical current density for Fe(Se,Te) bicrystal junctions (open symbols Si et al. [50], full symbols Sarnelli et al. [72])

investigating whether or not intrinsic effects, such as thermally activated phase slippage [74], play a role in such behaviour. Based on the experimental results above, the authors concluded that the critical angle θ_c was around 9°. The level of J_c^{GB} is almost constant above 24° [72].

10.3.4 Summary and Discussion

As can be seen in Figs. 10.11, 10.12, and 10.13, for all FBS, the critical angle θ_c is around 9°, which indicates that in-plane misorientation alignments of FBS grains less than 9° usually do not impede the current flow. Therefore, grain boundary networks whose in-plane misorientation spread is less than 9° can be expected to work as flux pinning centres (see below) and the texture requirements for high current carrying capabilities is less sever for FBS than for YBCO. For the cuprates, critical angles between of 0° [14, 75] and 2–5° [13, 76, 77], seldom 7° [78] were found, often a value around 4–5° is taken as reasonable upper bound.

The exponential decay of J_c with GB angle above the critical angle is very similar for the cuprates and FBS [62], in contrast to early analyses which concluded a much slower decay. A distinct difference, however, between FBS and YBCO is recognized above 24°: whereas for the cuprates, J_c^{GB}/J_c^{Grain} continues to decreases exponentially with θ_{GB}, it remains constant for FBS. This can only partially be attributed to the different order parameter symmetry since only up to one third of the whole J_c decrease is explained by order parameter symmetry in cuprates [16]. What might also play a large role is that the grain boundaries in FBS are of metallic nature; band bending, strain effects, and charge carrier depletion though present might be

less severe. Furthermore, 24° and 45° [001]-tilt GBs in the tetragonal Ba122 and Fe(Se,Te) compounds are special, low-Σ GBs with a narrower structurally and electronically disturbed region than GBs with slightly different angles (this has been discussed for some high-current 45° GBs in YBCO as well, see [79]). It is plausible that the widths of 24° and 45° GBs as low-Σ GBs are similar and J_c is only affected by these structural parameters in FBS in contrast to the cuprates. To clarify this, 36° GBs (as another low-Σ GB) as well as intermediate angles should be investigated. The in-plane coherence length ξ_{ab} of cuprates [80] and Fe-based superconductors [6] are with $\sim$1.2 . . . 2.5 nm quite comparable, which may explain the similar slope of $J_c(\theta_{GB})$ for θ_{GB} only slightly larger than θ_c [62].

Due to the exceptionally high J_c values in P-doped Ba122 films [70], this compound also showed a high inter-grain J_c of 1 MA/cm^2 at $\theta_{GB} = 24°$, which is very promising for wire applications. Furthermore, ${J_c}^{GB}$ for Ba122 is higher than for YBCO beyond 24°. Although P-doped Ba122 shows both higher intra- and inter-grain J_c than Co-doped Ba122, their normalized angle dependence of ${J_c}^{GB}$ are similar, Fig. 10.12. The same holds for the Fe(Se,Te) films: even though the absolute values are below Ba122 most likely due to the lower T_c, the intra-grain-normalized ${J_c}^{GB}$ is very similar.

For YBCO, the inter-grain J_c can be ameliorated by Ca-doping since it decreases the carrier density depletion at GBs [81], due to inhomogeneous and non-monotonic Ca segregation in the grain boundary with local channels of T_c enhancement [82] (here $YbBa_2Cu_3O_7$) and/or structural expansion of the dislocation cores [83]. On the contrary, Co-overdoped $BaFe_2As_2$ 12° bicrystals did not show better performance than optimally doped films [19]. This might be explained by the lower influence of indirect, electronic reasons for the J_c decrease rather than direct, structural ones. However, detailed studies of the doping dependence of ${J_c}^{GB}$ would be necessary to clarify this.

Talantsev and Crumb [84] very recently developed a model for estimating whether or not J_c of a quasi-two-dimensional superconducting film is limited by weak links. They combined their earlier model on self-field J_c depending solely on penetration depth and geometric factors [85] with the 2D fluctuation temperature of Emery and Kivelson [86] to obtain

$$J_{c,2Dfluct} = \frac{\pi^3 \cdot \mu_0^{\frac{1}{2}} \cdot k_B^{\frac{3}{2}}}{\phi_0^2} \cdot \ln(\kappa + 0.5) + \left(\frac{T_c}{d}\right)^{\frac{3}{2}}$$

where μ_0 is the vacuum permeability, k_B the Boltzmann constant, ϕ_0 the flux quantum, κ the Ginzburg-Landau parameter, and d the interlayer spacing. If J_c is below this value, it is likely affected by weak links. It would be worth checking the effectiveness of this model also on polycrystalline and bicrystal FBS films.

10.4 Grain Boundary Networks in Fe-Based Superconducting Films

Grain boundary networks are mostly studied in films on polycrystalline, technical substrates, i.e. in proof-of-principle studies on coated conductor FBS samples. Such studies have been performed in all three crystal structure classes potentially relevant for applications—*11*, *122*, and *1111*, for a review see [62]. Nevertheless, also films on single crystals may contain GBs, either due to mere fibre texture for ex situ grown $Ba_{0.6}K_{0.4}Fe_2As_2$ [87] and PLD-grown FeSe film [88] on *c*-cut sapphire or due to anisotropic and highly 3D growth in sputtered FeSe films on (110)-cut $SrTiO_3$ [89].

Also the studies on GB networks suggest that clean GBs with angles below ∼9° do not impede the current flow but occasionally even contribute to flux pinning. As summarized in Table 10.2, self-field J_c for a certain composition is influenced by the texture quality but also by T_c. J_c is in most cases rather isotropic with a ratio between $\boldsymbol{B}||\boldsymbol{ab}$ and $\boldsymbol{B}||\boldsymbol{c}$ of not more than 2 at 9 T, 4 K. In the following, these studies and data are discussed with respect to J_c limitation and flux pinning properties.

10.4.1 Polycrystalline Films on Single Crystals and Amorphous Templates

LaFeAs(O,F) The first weak-link studies on polycrystalline FBS films were conducted by Haindl et al. [91] on a PLD-grown and ex situ annealed LaFeAs(O,F) film on $LaAlO_3$ single crystal. The untextured film showed a rather broad transition ($T_{c90} = 28$ K, $T_{c0} = 20$ K), strong granularity effects in $R(T)$ in applied magnetic fields, and self-field J_c values as low as 2 kA/cm^2 at 2 K. This can be compared to a later epitaxial LaFeAs(O,F) film ($T_{c90} = 23$ K, $T_{c0} = 17$ K) grown by the same method which showed a self-field J_c of around 80 kA/cm^2 at 4 K [106].

$Ba_{0.6}K_{0.4}Fe_2As_2$ Hong et al. [87, 92] were recently able to prepare a 100 nm wide nanobridge across an individual, naturally formed GB in a ∼400 nm thick polycrystalline $Ba_{0.6}K_{0.4}Fe_2As_2$ film on c-cut sapphire. The film had strong *c*-axis texture, which means the GBs are predominantly of [001]-tilt type. Even though the GB junction showed clear Josephson coupling with resistively shunted junction (RSJ) behaviour with multiple transitions, $J_c{}^{GB}$ values for two of such bridges were estimated to ∼1.25 MA/cm^2 [92] and 0.2 MA/cm^2 [87] at 4.2 K, which is comparable to the intra-grain J_c or to bicrystal values at medium angles for P-doped Ba122, respectively. Although θ_{GB} of the investigated GBs are unknown, the results suggest that $J_c(\theta_{GB})$ is similar in magnitude for $BaFe_2(As,P)_2$ and $(Ba,K)Fe_2As_2$.

FeSe, Fe(Se,Te) The same method of nanobridge preparation was also applied on a (101)-oriented polycrystalline FeSe film on c-cut sapphire [88]. The $I(V)$ curves of the multigrain nanobridge showed flux flow and Josephson junction behaviour with strong thermal effects. Schneider et al. [89] recently prepared polycrystalline

Table 10.2 Summary of structural (in-plane, $\Delta\phi$, and out-of-plane, $\Delta\omega$, texture spread) and superconducting properties (critical temperature T_c for zero resistance and onset of transition as well as critical current density J_c at 4 K for self-field and 9 T for $\boldsymbol{B}||\boldsymbol{c}$ and $\boldsymbol{B}||\boldsymbol{ab}$) of FBS films with GB networks

Composition	Template	Method	$\Delta\phi$ (°)	$\Delta\omega$ (°)	T_{c0}/T_c^{onset} (K)	J_c^{sf} (MA/cm^2)	J_c(9T) $\boldsymbol{B}||\boldsymbol{c}/\boldsymbol{B}||\boldsymbol{ab}$ (MA/cm^2)	References
NdFeAs(O,F)	IBAD I	MBE	3.4	1.7	37/43	0.07	–	[90]
LaFeAs(O,F)	$LaAlO_3$	PLD*	poly	–	20/28	0.001	–	[91]
$Ba_{0.6}K_{0.4}Fe_2As_2$	c-Al_2O_3	PLD*	–	–	27/37	1.25^s	–	[92]
					31/37.5	0.2^s	–	[87]
$Ba(Fe,Co)_2As_2$	IBAD II	PLD	5.1	–	17.5/22	0.1 (8K)	0.003 (8 K)/–	[93]
			1.7	–	22/23	2.0	0.13/0.20	[94]
	IBAD I		3.2	1.5	20/22	1.2	–	[95]
			3.3	–	20/22	1.6	0.09/0.20	[95]
			3.5	–	20/22	3.6	–	[95]
	IBAD III		5.6	2.4	19.0/20.2	1.14	0.86/0.96	[96]
	Fe/LSAT	1.2$^{(45)}$		0.45	21.0/23.2	–	0.02/0.06 (12 K)	[71]
	Fe/MgO	PLD	1–2$^{(45,\ 110)}$		–	0.006	0.0006	[97]

(continued)

Table 10.2 (continued)

Composition	Template	Method	$\Delta\phi$ (°)	$\Delta\omega$ (°)	T_{c0}/T_c^{onset} (K)	J_c^{sf} (MA/cm^2)	J_c(9T) $\boldsymbol{B}\|\|\boldsymbol{c}/\boldsymbol{B}\|\|\boldsymbol{ab}$ (MA/cm^2)	References
$BaFe_2(As,P)_2$	IBAD I	PLD	2.7	1.3	23/26	1.0	0.08/0.09	[98]
			8.0	1.3	19/23	1.1	0.13/0.15	[98]
			5.7	1.2	26/28.3	4.0	0.2/0.3	[99]
	IBAD I	PLD^{rtr}			24/26	0.175	–	[100]
	IBAD I				18/21	0.047	–	[100]
FeSe	c-Al_2O_3	PLD	–$^{(101)}$		6.0/10.0	0.005^{n}	–	[88]
	(110)STO	sputtering	3.4/10.7$^{\#}$	3.4	7.5/10.8	0.005/0.014$^{\#}$	–	[89]
$FeSe_{0.5}Te_{0.5}$	Glass	PLD			8/10	0.014	–	[101]
	IBAD I	PLD	4.5	3.5	11/∼14.5	0.2	0.1/0.15	[102]
	IBAD III	PLD	7.8	3.4	14.9/16	0.43	0.38/0.39	[103]
	RABiTS II	PLD	6.0		18.6/20	1.5	0.45/0.55	[104]
	RABiTS III	PLD	4.9	6.6	18.2/16.5	0.16	0.04/0.04	[105]
$FeSe_{0.1}Te_{0.9}$	Glass	PLD			10 /12.3	0.021	–	[101]
	SS	PLD			5 / 10	0.013	–	[101]

*Two-step process, ^{s}single GB, $^{(45)}$plus in-plane 45° rotated component, $^{(110)}$plus (110) component, $^{(101)}$predominantly (101) fibre texture, ^{rtr}reel-to-reel, ^{n}nanobridge, $^{\#}$for $\boldsymbol{j}\|\|[1\text{–}10]_{STO}$ and $\boldsymbol{j}\|\|[001]_{STO}$, IBAD I: MgO/Y_2O_3/Hastelloy, II: Fe/MgO/Y_2O_3/Hastelloy, III: $SrTiO_3/LaMnO_3/MgO/Y_2O_3$/Hastelloy, RABiTS I: Ni5%W, II: CeO_2/Y_2O_3/YSZ/CeO_2/Ni5%W, III: CeO_2/Ni5%W

FeSe films with anisotropic grain structure on (110)-oriented $SrTiO_3$ single crystals. The film is strongly biaxially (001)-oriented with small amounts of misoriented (<3%) and hexagonal α-FeSe (<8%) grains. The grains are elongated along the [001] direction of the substrate, and the in-plane texture spread in this direction is with $\Delta\phi = 3.4°$ much smaller than in the transverse direction ($\Delta\phi = 10.7°$). Since the latter is slightly larger than the critical angle θ_c, the resistivity shows a tail at low temperatures which is related to the granularity. For pinning properties of these films, see below. These films show significantly higher J_c values in all fields and temperatures as well as lower resistivities for currents applied parallel to the larger grain dimension (H) than perpendicular to it (V), Fig. 10.14. This effect can be explained by the higher GB density for currents perpendicular to the long axis and has been predicted [107] and shown [108] for cuprate coated conductors with elongated grains, where in contrast to the FeSe films the GBs acted as weak links. For both current directions, F_p could be well described with a parameter set of $(p,q) = (0.5, 2)$ which clearly indicated that surfaces, i.e. the grain boundaries dominated the pinning properties.

Huang et al. [101] prepared $Fe(Se_{1-x}Te_x)$ films with $x = 0.5$, 0.9, and 1.0 on glass as well as with $x = 0.5$ on stainless steel (SS) tape covered with amorphous Al_2O_3 (a-Al_2O_3). All films showed strong (001) c-axis texture with local biaxial orientation, i.e. [001] tilt GB networks. T_c^{onset} values of these films were ~12, 12.3, 10, and 10 K, respectively, where the FeTe film on glass and the film on a-Al_2O_3/SS showed a higher transition width (4–5 K) due to the broader in-plane texture spread. Self-field J_c of the films with $x = 0.5$ and 0.9 on glass and the film on a-Al_2O_3/SS are

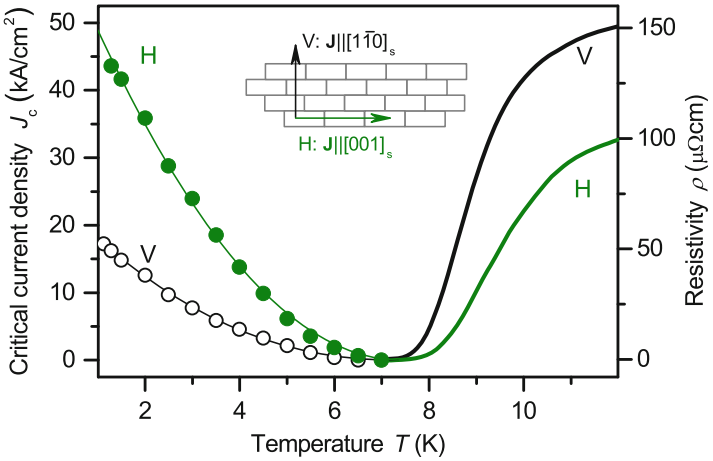

Fig. 10.14 Self-field J_c (left scale) and resistivity (right scale) vs. temperature for a bridge along the grains (j||[001]$_{STO}$, H, red) and across the grains (j||[1–10]$_{STO}$, V, blue) of a sputtered FeSe film on (110)-oriented $SrTiO_3$ [89]. Data courtesy of R. Schneider

with 21, 14, and 13 kA/cm^2 comparable to each other and one order of magnitude larger than bulk values.

10.4.2 Films on IBAD-MgO Templates

Most proof-of-principle studies of FBS coated conductors have been performed on IBAD-MgO templates supplied by iBeam Materials Inc., USA, or Shanghai Creative Supercond. Technol. Co Ltd., China.

NdFeAs(O,F) Only in 2014 have biaxially textured NdFeAs(O,F) films on technical substrates been fabricated by MBE at Nagoya University [90]. The film on IBAD-MgO template contained a small amount of 45° rotated grains and showed otherwise epitaxial growth. It had a self-field J_c of 70 kA/cm^2 at 5 K, only slightly larger than for a recent partially textured PIT-processed SmFeAs(O,F) tape [37] of around 40 kA/cm^2 at 4.2 K and 1.5 orders of magnitude lower than a film on MgO single crystal (3 MA/cm^2) [109]. The reason for the low J_c values on IBAD templates is most likely the strong F diffusion in the GB regions and hence formation of current-blocking foreign phases, as revealed by bicrystal experiments [28], as discussed in Sect. 10.3.1.

Ba(Fe,Co)$_2$As$_2$ Already in 2011, we fabricated Co-doped Ba122 films on Fe-buffered IBAD-MgO templates by PLD [93]. Due to the relatively large in-plane mosaicity of the MgO of around 6°, the crystalline quality of Fe buffer and superconducting layer was poor (both ∼5°). Although the biaxially textured Co-doped Ba122 film showed an onset T_c of 22 K ($T_{c0} = 17.5$ K), J_c at low temperatures (0.1 MA/cm^2 at 8 K 0 T) was almost one order of magnitude lower than on single crystalline MgO. Later, employing a high-quality MgO template (2.4° in-plane spread) avoided to strong granularity, Fig. 10.15, and improved J_c almost to the level of single crystalline substrates [94]. At the same time, Katase et al. reported on the fabrication of Co-doped Ba122 *directly* on IBAD-MgO [95]. Due to the self-epitaxy effect, a sharp texture (∼3.2–3.5°) of the superconducting layer was obtained irrespective of the in-plane mosaicity of MgO templates.

GBs in FBS are, though J_c limiting in general, *advantageous* for two reasons: First, their larger critical angle θ_c compared to the cuprates allows using less-textured coated conductor architectures [7] or bulk samples and wires. Secondly, GBs can furthermore be advantageous for high current carrying capabilities since they may contribute to flux pinning [95]: Ba(Fe,Co)$_2$As$_2$ films grown on IBAD-MgO templates of different (in-plane) texture quality (5.5°, 6.1°, 7.3°) which led to Ba122 texture spreads of 3.1°, 3.2°, and 3.5° showed a strong positive correlation between texture spread and self-field J_c (1.2, 1.6, 3.6 MA/cm^2). This can be explained by the GB angles being below θ_c (strong links) and an increasing dislocation density for larger misorientations. This is evidenced by the fact that the film on IBAD-MgO (6.1°) shows J_c(B||c) values higher than for a comparable film

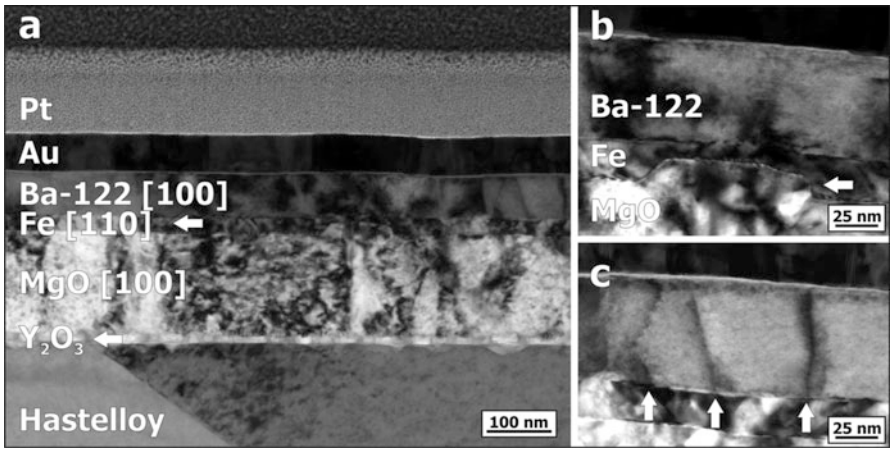

Fig. 10.15 Bright-field TEM images of a $Ba(Fe,Co)_2As_2$ film on Fe-buffered IBAD-MgO template, see also [94]. (**a**) Overview of the complete sample stack. (**b**) MgO step (white arrow) is overgrown by the Fe buffer layer, resulting in a sharp interface between Fe and Ba122. (**c**) Vertical defects (arrows)separated by ∼20–40 nm penetrate the whole Ba122 film and may be identified as GBs. Image courtesy of E. Reich

on MgO single crystal for all fields at 4 and 12 K, and also higher than $J_c(B||ab)$ up to a temperature-dependent cross-over field.

Recently, Xu et al. fabricated Co-doped Ba122 on $SrTiO_3$/$LaMnO_3$-buffered IBAD-MgO [96]. The film with $T_c = 20.2$ K ($T_{c0} = 19.0$ K) showed almost isotropic J_c at 4.2 K with 0.86 and 0.96 MA/cm^2 at 9 T and for $\boldsymbol{B}||\boldsymbol{c}$ and $\boldsymbol{B}||\boldsymbol{ab}$, respectively, and self-field J_c of 1.14 MA/cm^2.

$BaFe_2(As,P)_2$ Also P-doped Ba122 films have been prepared on IBAD-MgO. Sato et al. deposited such films on templates with different in-plane spread, 4° and 8° [98]. As expected, the crystalline quality of the film on the 4° template was better; the 8° film showed several misorientations and a larger density of *c*-axis correlated defects besides the larger in-plane spread. Whereas T_c of the 8° film was 3 K lower which is caused by the strain effects [99], its self-field J_c at 4 K was comparable to the 4° sample (∼1 MA/cm^2). For both samples, EDX scans in TEM cross sections revealed clean and homogeneous GB regions, and plane-view TEM revealed a grain size of ∼100 nm and dislocation arrays in the GB regions, Fig. 10.16. Even though T_c of the 8° sample was reduced, it showed a stronger *c*-axis peak and J_c values overall higher by a factor of 1.5 than the well-textured sample. This can be explained by the much larger density of vertical defects in that sample which are related to the GB networks. At higher temperatures and fields (e.g. 12 K, 9 T), the well-textured sample takes over due to higher T_c and hence H_{irr} value; however, the less-textured sample continues to exhibit the stronger *c*-axis peak.

One of these samples on the 8° IBAD template with improved T_c was later investigated in high fields [99]. Analysis of the pinning force density curves, $F_p(B)$,

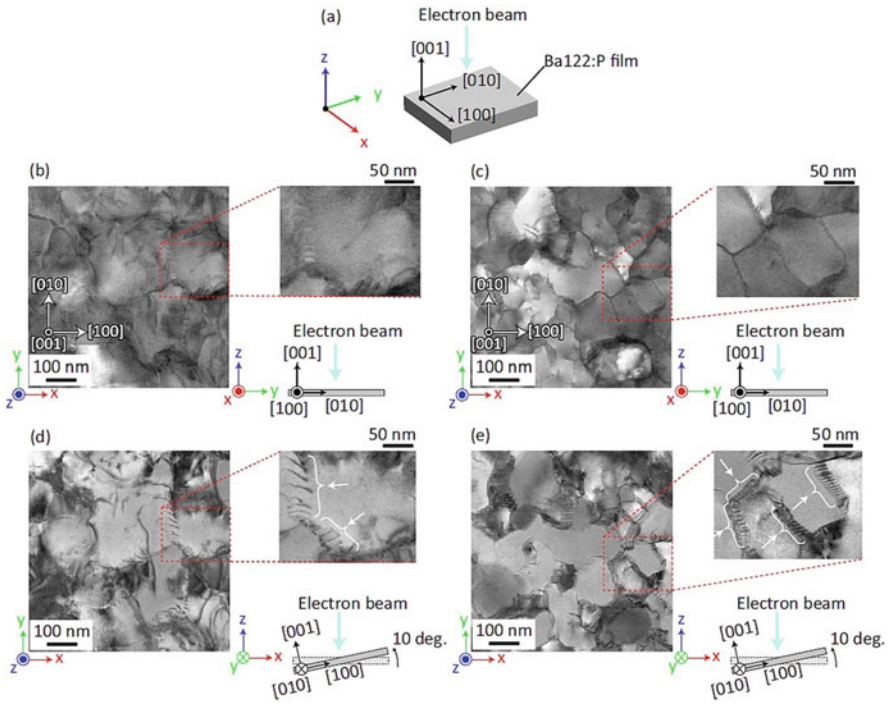

Fig. 10.16 Plane-view bright-field STEM images of $BaFe_2(As,P)_2$ films on two IBAD templates with $\Delta\varphi_{MgO} = 4°$ and 8°. (**a**) Relationship between film orientation, incident electron beam, and global axes (*X*, *Y*, and *Z*). (**b**, **c**) Typical plane-view images by normal electron beam incidence for $\Delta\varphi_{MgO} = 4°$ (**b**) and 8° (**c**). (**d**, **e**) Slanted-angle images (tilting by 10°) for visualizing dislocations at same areas of (**b**, **c**), respectively. The arrows in the top right image of (**d**, **e**) show arrays of dislocations. Reprinted from [98] with permission by the authors under Creative Commons Attribution 4.0 International License

with modified Dew-Hughes functions, $F_p \sim b^p(1-b)^q$, $b = B/B_{irr}$, suggested in analogy to low-temperature superconductors that pinning is strongly dominated by surface pinning (p, $q = 0.5$, 2), i.e. on two-dimensional defects in the matrix, which was attributed to the GB and dislocation networks. The voltage-current characteristics showed a clear cross-over field between GB limitation [non-ohmic linear differential (NOLD) curves] at low fields and pinning limitation (power laws) at high fields. Similar NOLD characteristics have been measured for $Ba(Fe,Co)_2As_2$ films with 45° and (110) misorientations [97] and polycrystalline $SmFeAsO_{0.85}$ [22].

A 10 cm long P-doped Ba122 tape has also been prepared by PLD with a reel-to-reel system [100], yet without fully optimized growth conditions. The film showed a slightly reduced T_{c0} compared to the static samples and a rather low I_c of 0.47 mA per cm-width at 4.2 K, corresponding to a J_c of 47 kA/cm^2. To improve the superconducting properties, Fe_3P/P-doped Ba122 bilayers on IBAD-MgO were

tested. As a result, the superconducting properties were improved to $T_{c0} = 24$ K and $I_c = 975$ mA per cm-width ($J_c = 175$ kA/cm^2) at 4.2 K.

Fe(Se,Te) Despite the large lattice mismatch between Fe(Se,Te) and MgO of 9.5%, Si et al. were able to grow epitaxial Fe(Se,Te) thin films on Hastelloy tapes with IBAD-MgO buffer architecture [102]. The respective in-plane and out-of-plane full width at half maximum of Fe(Se,Te) were $\Delta\phi = 4.5°$ ($<\theta_c$) and $\Delta\omega = 3.5°$. [010]-tilt GBs have probably a similar critical angle in FBS due to the small anisotropy and *s*-wave-type symmetry. Therefore, weak-link behaviour is not observed in these films. The lower $T_{c0} = 11$ K of that film compared to the film on $LaAlO_3$ substrate ($\sim$15 K) is most likely due to the lattice misfit and led to a low self-field J_c at 4 K of 0.2 MA/cm^2. Xu et al. also grew Fe(Se,Te) cube-textured thin films on IBAD-MgO with $LaMnO_3$ buffer layer [103]. T_c was 15.8 K, which is slightly larger than the bulk value due to compressive strain. Whereas the out-of-plane spread with $\Delta\omega = 3.4°$ was similar to the film of Si et al., the in-plane spread of $\Delta\phi = 7.8°$ was considerably larger and close to θ_c. Nevertheless, the self-field J_c was 0.43 MA/cm^2 at 4.2 K.

10.4.3 Films on RABiTS Substrates

To date, only Fe($Se_{1-x}Te_x$) films ($x = 0$, 0.5) have been prepared on RABiTS templates, supplied by evico, ENEA, and ORNL.

Si et al. deposited Fe(Se,Te) thin films by PLD on CeO_2-buffered RABiTS [104]. The (110) lattice parameter of CeO_2 is around 3.82 Å, very close to Fe(Se,Te). Therefore, the film on RABiTS showed a high T_c of $\sim$20 K with sharp transition. Despite the larger in-plane texture spread of 6°, which corresponds to the underlying template (7°), the film was capable of carrying large current densities (self-field $J_c = 1.5$ MA/cm^2 at 4.2 K). The authors concluded that CeO_2 as buffer has a larger impact on the superconducting properties of Fe(Se,Te) than the texture quality, i.e. LAGBs up to 7° do not hinder the critical current flow, in contrast to the cuprates. In an attempt to reduce the necessary number of buffer layers, Sylva et al. deposited Fe(Se,Te) by PLD on Ni5W with a single CeO_2 buffer layer in order to possibly reduce manufacturing costs of FSB coated conductors [105]. The film with a T_c of $\sim$18 K showed a self-field J_c of $\sim$0.16 MA/cm^2 as well as isotropic J_c above 20 kA/cm^2 in fields up to 18 T at 4.2 K. In contrast to Ba122, pinning is much more dominated by point-like disorder in Fe(Se,Te) films on IBAD [102] (p, $q = 1$, 2) and RABiTS [104] (p, $q = 0.85$, 2) which was attributed to Se-Te disorder.

Demura, Yamashita et al. proposed electrochemical deposition (ECD) as another, potentially economical method for producing FeSe films on RABiTS tapes [110, 111] and showed superconducting films with T_{c0} of 2.5 K. This process might be interesting with regard to low-cost production of FeSe coated conductors if further optimized.

10.5 Conclusion

We reviewed grain boundary characteristics of Fe-based superconductors in the form of polycrystalline bulks and thin films. A large difference in inter-grain J_c between polycrystalline bulk samples and bicrystal films indicates that the global currents in bulk samples are significantly affected by extrinsic factors. These extrinsic factors were identified by microstructural analysis as FeAs wetting of grains and cracks. The inter-grain J_c does not severely decrease at clean grain boundaries. Hence, eliminating extrinsic factors is a key to enhance the inter-grain J_c in polycrystalline samples.

Bicrystal experiments revealed the critical angle θ_c for FBS to be around 9°, which is around twice as large as for the cuprates. Similar to the cuprates, the critical angle may be governed by geometrical factors (i.e. the electronically disturbed region around dislocations is smaller in FBS due to their metallic nature) and by the symmetry of the order parameter: ($s\pm$ in FBS instead of d-wave in cuprates). Another distinct difference is that the inter-grain J_c for FBS is almost constant above $\theta_{GB} > 24°$, whereas for the cuprates the inter-grain J_c is reduced exponentially with θ_{GB} above θ_c. Grain boundaries with misorientation angles less than θ_c act as pinning centres. Hence, increasing the density of such GBs improves the current carrying capability.

Although we learned all of the above already from experimental facts, the fundamental understanding of GBs in FBS is still insufficient. For instance, (1) the mechanism of exponential decay for inter-grain J_c above θ_c, (2) the large θ_c value of around 9°, (3) the reason for the constant inter-grain J_c for $\theta_{GB} > 24°$, and (4) the transition of Abrikosov vortices via Abrikosov-Josephson vortices to pure Josephson vortices for $\theta_{GB} \sim \theta_c$ at certain fields and temperatures are not well understood. To address those issues, further investigations on grain boundaries are required.

Acknowledgments We sincerely thank Chiara Tarantini for her careful proof-reading and editing of our manuscript. We thank A. Yamamoto, R. Schneider, E. Reich, and H. Hiramatsu for information on and data for Figs. 10.5 and 10.14–10.16. We acknowledge Grant-in-Aid for Scientific Research (B) (Grant No. 16H04646) from the Japan Society for the Promotion of Science, JST CREST (Grant No. JPMJCR18J4), and the Helmholtz Association via the Recruitment Initiative of Prof. B. Holzapfel for financial support.

References

1. Y. Kamihara, H. Hiramatsu, M. Hirano, et al., Iron-based layered superconductor: LaOFeP. J. Am. Chem. Soc. **128**(31), 10012–10013 (2006). https://doi.org/10.1021/ja063355c
2. Y. Kamihara, T. Watanabe, M. Hirano, et al., Iron-based layered superconductor $La[O_{1-x}F_x]FeAs$ ($x = 0.05-0.12$) with $T_c = 26$ K. J. Am. Chem. Soc. **130**(11), 3296–3297 (2008). https://doi.org/10.1021/ja800073m

3. I.I. Mazin, D.J. Singh, M.D. Johannes, et al., Unconventional superconductivity with a sign reversal in the order parameter of $LaFeAsO_{1-x}F_x$. Phys. Rev. Lett. **101**(5), 057003 (2008). https://doi.org/10.1103/PhysRevLett.101.057003
4. K. Kuroki, S. Onari, R. Arita, et al., Unconventional pairing originating from the disconnected Fermi surfaces of superconducting $LaFeAsO_{1-x}F_x$. Phys. Rev. Lett. **101**(8), 087004 (2008). https://doi.org/10.1103/PhysRevLett.101.087004
5. T. Hanaguri, S. Niitaka, K. Kuroki, et al., Unconventional *s*-wave superconductivity in Fe(Se,Te). Science **328**(5977), 474–476 (2010). https://doi.org/10.1126/science.1187399
6. M. Putti, I. Pallecchi, E. Bellingeri, et al., New Fe-based superconductors: properties relevant for applications. Supercond. Sci. Technol. **23**(3), 034003 (2010). https://doi.org/10.1088/0953-2048/23/3/034003
7. T. Katase, Y. Ishimaru, A. Tsukamoto, et al., Advantageous grain boundaries in iron pnictide superconductors. Nat. Commun. **2**(1), 409 (2011). https://doi.org/10.1038/ncomms1419
8. H. Hilgenkamp, J. Mannhart, Grain boundaries in high-T_c superconductors. Rev. Mod. Phys. **74**(2), 485–549 (2002). https://doi.org/10.1103/RevModPhys.74.485
9. L. Priester, *Grain Boundaries. Springer Series in Materials Science*, vol 172 (Springer, Dordrecht, 2013)
10. R.Z. Valiev, V.Y. Gertsman, O.A. Kaibyshev, Grain boundary structure and properties under external influences. Phys. Stat. Sol. **97**(1), 11–56 (1986). https://doi.org/10.1002/pssa.2210970102
11. P. Lejček, *Grain Boundary Segregation in Metals. Springer Series in Materials Science*, vol 136 (Springer, Berlin, 2010)
12. R.M. Scanlan, W.A. Fietz, E.F. Koch, Flux pinning centers in superconducting Nb_3Sn. J. Appl. Phys. **46**(5), 2244 (1975). https://doi.org/10.1063/1.321816
13. D.T. Verebelyi, D.K. Christen, R. Feenstra, et al., Low angle grain boundary transport in $YBa_2Cu_3O_{7-\delta}$ coated conductors. Appl. Phys. Lett. **76**(13), 1755–1757 (2000). https://doi.org/10.1063/1.126157
14. T. Amrein, L. Schultz, B. Kabius, et al., Orientation dependence of grain-boundary critical current densities in high-T_c bicrystals. Phys. Rev. B **51**(10), 6792–6795 (1995). https://doi.org/10.1103/PhysRevB.51.6792
15. J. Ayache, Grain boundaries in high temperature superconducting ceramics. Philos. Mag. **86**(15), 2193–2239 (2006). https://doi.org/10.1080/14786430600640494
16. H. Hilgenkamp, J. Mannhart, B. Mayer, Implications of $d_{x2\text{-}y2}$ symmetry and faceting for the transport properties of grain boundaries in high-T_c superconductors. Phys. Rev. B **53**(21), 14586 (1996). https://doi.org/10.1103/PhysRevB.53.14586
17. T. Horide, K. Matsumoto, Evaluation of vortex pinning across low angle grain boundary in $YBa_2Cu_3O_7$ film. Appl. Phys. Lett. **101**(11), 112604 (2012). https://doi.org/10.1063/1.4752462
18. G. Deutscher, Origin of weak-link behavior of grain boundaries in superconducting cuprates and pnictides. Appl. Phys. Lett. **96**(12), 122502 (2010). https://doi.org/10.1063/1.3367723
19. J.H. Durrell, C.-B. Eom, A. Gurevich, et al., The behavior of grain boundaries in the Fe-based superconductors. Rep. Prog. Phys. **74**(12), 124511 (2011). https://doi.org/10.1088/0034-4885/74/12/124511
20. P. Seidel, Josephson effects in iron based superconductors. Supercond. Sci. Technol. **24**(4), 043001 (2011). https://doi.org/10.1088/0953-2048/24/4/043001
21. F. Kametani, A.A. Polyanskii, A. Yamamoto, et al., Combined microstructural and magneto-optical study of current flow in polycrystalline forms of Nd and Sm Fe-oxypnictides. Supercond. Sci. Technol. **22**(1), 015010 (2009). https://doi.org/10.1088/0953-2048/22/1/015010
22. F. Kametani, P. Li, D. Abraimov, et al., Intergrain current flow in a randomly oriented polycrystalline $SmFeAsO_{0.85}$ oxypnictide. Appl. Phys. Lett. **95**(14), 142502 (2009). https://doi.org/10.1063/1.3224198
23. A. Yamamoto, A.A. Polyanskii, J. Jiang, et al., Evidence for two distinct scales of current flow in polycrystalline Sm and Nd iron oxypnictides. Supercond. Sci. Technol. **21**(9), 095008 (2008). https://doi.org/10.1088/0953-2048/21/9/095008

24. D.C. Larbalestier, M. Daeumling, X. Cai, et al., Experiments concerning the connective nature of superconductivity in $YBa_2Cu_3O_7$. J. Appl. Phys. **62**(8), 3308–3313 (1987). https://doi.org/10.1063/1.339339
25. A. Yamamoto, J. Jiang, F. Kametani, et al., Evidence for electromagnetic granularity in polycrystalline Sm1111 iron-pnictides with enhanced phase purity. Supercond. Sci. Technol. **24**(4), 045010 (2011). https://doi.org/10.1088/0953-2048/24/4/045010
26. M. Eisterer, M. Zehetmayer, H.W. Weber, et al., Disorder effects and current percolation in FeAs-based superconductors. Supercond. Sci. Technol. **23**(5), 054006 (2010). https://doi.org/10.1088/0953-2048/23/5/054006
27. E.S. Otabe, M. Kiuchi, S. Kawai, et al., Global and local critical current density in superconducting $SmFeAsO_{1-x}F_x$ measured by two methods. Phys. C Supercond. Appl. **469**(21), 1940–1944 (2009). https://doi.org/10.1016/j.physc.2009.06.013
28. T. Omura, T. Matsumoto, T. Hatano, et al., Fabrication of grain boundary junctions using NdFeAs(O,F) superconducting thin films. J. Phys. Conf. Ser. **1054**(1), 012024 (2018). https://doi.org/10.1088/1742-6596/1054/1/012024
29. K. Iida, T. Omura, T. Matsumoto, et al., Grain boundary characteristics of oxypnictide NdFeAs(O,F) superconductors. Supercond. Sci. Technol. **32**(7), 074003 (2019) https://doi.org/10.1088/1361-6668/ab1660
30. Q. Zhang, C. Wang, C. Yao, et al., Combined effect of Sn addition and post-rolling sintering on the superconducting properties of $SmFeAsO_{1-x}F_x$ tapes fabricated by an ex-situ powder-in-tube process. J. Appl. Phys. **113**(12), 123902 (2013). https://doi.org/10.1063/1.4795814
31. L. Wang, Y. Qi, D. Wang, et al., Low-temperature synthesis of $SmFeAsO_{0.7}F_{0.3-\delta}$ wires with a high transport critical current density. Supercond. Sci. Technol. **23**(7), 075005 (2010). https://doi.org/10.1088/0953-2048/23/7/075005
32. C. Wang, C. Yao, H. Lin, et al., Large transport J_c in Sn-added $SmFeAsO_{1-x}F_x$ tapes prepared by an ex situ PIT method. Supercond. Sci. Technol. **26**(7), 075017 (2013). https://doi.org/10.1088/0953-2048/26/7/075017
33. Q. Zhang, C. Yao, H. Lin, et al., Enhancement of transport critical current density of $SmFeAsO_{1-x}F_x$ tapes fabricated by an ex-situ powder-in-tube method with a Sn-presintering process. Appl. Phys. Lett. **104**(17), 172601 (2014). https://doi.org/10.1063/1.4874261
34. L. Wang, Y. Qi, D. Wang, et al., Large transport critical currents of powder-in-tube $Sr_{0.6}K_{0.4}Fe_2As_2$/Ag superconducting wires and tapes. Phys. C Supercond. Appl. **470**(2), 183–186 (2010). https://doi.org/10.1016/j.physc.2009.12.030
35. L. Wang, Y. Qi, Z. Zhang, et al., Influence of Pb addition on the superconducting properties of polycrystalline $Sr_{0.6}K_{0.4}Fe_2As_2$. Supercond. Sci. Technol. **23**(5), 054010 (2010). https://doi.org/10.1088/0953-2048/23/5/054010
36. Z. Gao, L. Wang, C. Yao, et al., High transport critical current densities in textured Fe-sheathed $Sr_{1-x}K_xFe_2As_2$+Sn superconducting tapes. Appl. Phys. Lett. **99**(24), 242506 (2011). https://doi.org/10.1063/1.3671109
37. Q. Zhang, X. Zhang, C. Yao, et al., Enhanced transport critical current density in Sn-added $SmFeAsO_{1-x}F_x$ tapes prepared by the PIT method. Supercond. Sci. Technol. **30**(6), 065004 (2017). https://doi.org/10.1088/1361-6668/aa6850
38. J.D. Weiss, C. Tarantini, J. Jiang, et al., High intergrain critical current density in fine-grain $(Ba_{0.6}K_{0.4})Fe_2As_2$ wires and bulks. Nat. Mater. **11**(8), 682–685 (2012). https://doi.org/10.1038/nmat3333
39. Y. Hayashi, A. Yamamoto, H. Ogino, et al., Influences of material processing on the microstructure and inter-granular current properties of polycrystalline bulk $Ba(Fe,Co)_2As_2$. Phys. C Supercond. Appl. **504**, 28–32 (2014). https://doi.org/10.1016/j.physc.2014.01.010
40. Y.-J. Kim, J.D. Weiss, E.E. Hellstrom, et al., Evidence for composition variations and impurity segregation at grain boundaries in high current-density polycrystalline K- and Co-doped $BaFe_2As_2$ superconductors. Appl. Phys. Lett. **105**(16), 162604 (2014). https://doi.org/10.1063/1.4898191

41. L. Wang, Y. Ma, Q. Wang, et al., Direct observation of nanometer-scale amorphous layers and oxide crystallites at grain boundaries in polycrystalline $Sr_{1-x}K_xFe_2As_2$ superconductors. Appl. Phys. Lett. **98**(22), 222504 (2011). https://doi.org/10.1063/1.3592580
42. J.D. Weiss, A. Yamamoto, A.A. Polyanskii, et al., Demonstration of an iron-pnictide bulk superconducting magnet capable of trapping over 1 T. Supercond. Sci. Technol. **28**(11), 112001 (2015). https://doi.org/10.1088/0953-2048/28/11/112001
43. X. Zhang, H. Oguro, C. Yao, et al., Superconducting properties of 100-m Class $Sr_{0.6}K_{0.4}Fe_2As_2$ tape and pancake coils. IEEE Trans. Appl. Supercond. **27**(4), 7300705 (2017). https://doi.org/10.1109/TASC.2017.2650408
44. Q.-P. Ding, S. Mohan, Y. Tsuchiya, et al., Magneto-optical imaging and transport properties of FeSe superconducting tapes prepared by the diffusion method. Supercond. Sci. Technol. **25**(2), 025003 (2012). https://doi.org/10.1088/0953-2048/25/2/025003
45. Y. Mizuguchi, K. Deguchi, S. Tsuda, et al., Fabrication of the iron-based superconducting wire using Fe(Se,Te). Appl. Phys. Express **2**(8), 083004 (2009). https://doi.org/10.1143/APEX.2.083004
46. Q.-P. Ding, S. Mohan, Y. Tsuchiya, et al., Low-temperature synthesis of $FeTe_{0.5}Se_{0.5}$ polycrystals with a high transport critical current density. Supercond. Sci. Technol. **24**(7), 075025 (2011). https://doi.org/10.1088/0953-2048/24/7/075025
47. T. Ozaki, K. Deguchi, Y. Mizuguchi, et al., Transport properties and microstructure of mono- and seven-core wires of $FeSe_{1-x}Te_x$ superconductor produced by the Fe-diffusion powder-in-tube method. Supercond. Sci. Technol. **24**(10), 105002 (2011). https://doi.org/10.1088/0953-2048/24/10/105002
48. T. Ozaki, Y. Mizuguchi, S. Demura, et al., Enhancement of superconducting properties in FeSe wires using a quenching technique. J. Appl. Phys. **111**(1), 013912 (2012). https://doi.org/10.1063/1.3673826
49. A. Palenzona, A. Sala, C. Bernini, et al., A new approach for improving global critical current density in $Fe(Se_{0.5}Te_{0.5})$ polycrystalline materials. Supercond. Sci. Technol. **25**(11), 115018 (2012). https://doi.org/10.1088/0953-2048/25/11/115018
50. W. Si, C. Zhang, X. Shi, et al., Grain boundary junctions of $FeSe_{0.5}Te_{0.5}$ thin films on $SrTiO_3$ bi-crystal substrates. Appl. Phys. Lett. **106**(3), 32602 (2015). https://doi.org/10.1063/1.4906429
51. D. Mancusi, M. Polichetti, M.R. Cimberle, et al., Influence of the interaction between the inter- and intragranular magnetic responses in the analysis of the ac susceptibility of a granular $FeSe_{0.5}Te_{0.5}$ superconductor. Supercond. Sci. Technol. **28**(9), 095017 (2015). https://doi.org/10.1088/0953-2048/28/9/095017
52. S.J. Singh, R. Beck, S. Wurmehl, et al., Granular behavior observed in the polycrystalline superconducting LiFeAs. Supercond. Sci. Technol. **28**(2), 025006 (2015). https://doi.org/10.1088/0953-2048/28/2/025006
53. S.J. Singh, H. Ogino, J.-I. Shimoyama, et al., Weak-link behaviour observed in iron-based superconductors with thick perovskite-type blocking layers. Supercond. Sci. Technol. **26**(10), 105020 (2013). https://doi.org/10.1088/0953-2048/26/10/105020
54. R.M. Costa, A.R. Jurelo, P. Rodrigues, et al., Splitting of the bulk resistive transition in high-T_c superconductors: evidence for unconventional pairing. Phys. C Supercond. Appl. **251**(1), 175–182 (1995). https://doi.org/10.1016/0921-4534(95)00399-1
55. T.T.M. Palstra, B. Batlogg, R.B. van Dover, et al., Dissipative flux motion in high-temperature superconductors. Phys. Rev. B **41**(10), 6621 (1990). https://doi.org/10.1103/PhysRevB.41.6621
56. S.J. Singh, M. Bristow, W.R. Meier, et al., Ultrahigh critical current densities, the vortex phase diagram, and the effect of granularity of the stoichiometric high-T_c superconductor $CaKFe_4As_4$. Phys. Rev. Mater. **2**(7), 074802 (2018). https://doi.org/10.1103/PhysRevMaterials.2.074802
57. C.C. Tsuei, J.R. Kirtley, Pairing symmetry in cuprate superconductors. Rev. Mod. Phys. **72**(4), 969–1016 (2000). https://doi.org/10.1103/RevModPhys.72.969

58. N. Yoshida, M. Kiuchi, E.S. Otabe, et al., Critical current density properties in polycrystalline $Sr_{0.6}K_{0.4}Fe_2As_2$ superconductors. Phys. C Supercond. Appl. **470**, 1216 (2010)
59. M. Nikolo, J.D. Weiss, J. Singleton, et al., Critical properties of bulk-doped $BaFe_2As_2$ pnictides for magnet design. IEEE Trans. Appl. Supercond. **28**(3), 7300104 (2018). https://doi.org/10.1109/TASC.2017.2775580
60. J. Hecher, T. Baumgartner, J.D. Weiss, et al., Small grains: a key to high-field applications of granular Ba-122 superconductors? Supercond. Sci. Technol. **29**(2), 025004 (2016). https://doi.org/10.1088/0953-2048/29/2/025004
61. M. Eisterer, Predicting critical currents in grain-boundary limited superconductors. Phys. Rev. B **99**(9), 094501 (2019). https://doi.org/10.1103/PhysRevB.99.094501
62. K. Iida, J. Hänisch, C. Tarantini, Fe-based superconducting thin films on metallic substrates: growth, characteristics, and relevant properties. Appl. Phys. Rev. **5**(3), 031304 (2018). https://doi.org/10.1063/1.5032258
63. R. Held, C.W. Schneider, J. Mannhart, et al., Low-angle grain boundaries in $YBa_2Cu_3O_{7-\delta}$ with high critical current densities. Phys. Rev. B **79**(1), 014515 (2009). https://doi.org/10.1103/PhysRevB.79.014515
64. Q. Jin, S.-W. Chan, Grain boundary faceting in $YBa_2Cu_3O_{7-x}$ bicrystal thin films on $SrTiO_3$ substrates. J. Mater. Res. **17**(2), 323–335 (2002). https://doi.org/10.1557/JMR.2002.0046
65. D.M. Feldmann, T.G. Holesinger, R. Feenstra, et al., A review of the influence of grain boundary geometry on the electromagnetic properties of polycrystalline $YBa_2Cu_3O_{7-x}$ films. J. Am. Ceram. Soc. **91**(6), 1869–1882 (2008). https://doi.org/10.1111/j.1551-2916.2008.02273.x
66. T. Kawaguchi, H. Uemura, T. Ohno, et al., Molecular beam epitaxy growth of superconducting NdFeAs(O,F) thin films using a F-Getter and a novel F-doping method. Appl. Phys. Exp. **4**(8), 083102 (2011). https://doi.org/10.1143/APEX.4.083102
67. S. Lee, J. Jiang, J.D. Weiss, et al., Weak-link behavior of grain boundaries in superconducting $Ba(Fe_{1-x}Cox)_2As_2$ bicrystals. Appl. Phys. Lett. **95**(21), 212505 (2009). https://doi.org/10.1063/1.3262953
68. H. Hiramatsu, T. Katase, Y. Ishimaru, et al., Microstructure and transport properties of [001]-tilt bicrystal grain boundaries in iron pnictide superconductor, cobalt-doped $BaFe_2As_2$. Mater. Sci. Eng. B **177**(7), 515–519 (2012). https://doi.org/10.1016/j.mseb.2011.12.009
69. K. Iida, S. Haindl, F. Kurth, et al., $BaFe_2As_2$/Fe bilayers with [001]-tilt grain boundary on MgO and $SrTiO_3$ bicrystal substrates. Phys. Proc. **45**, 189–192 (2013). https://doi.org/10.1016/j.phpro.2013.04.084
70. A. Sakagami, T. Kawaguchi, M. Tabuchi, et al., Critical current density and grain boundary property of $BaFe_2(As,P)_2$ thin films. Phys. C Supercond. Appl. **494**, 181–184 (2013). https://doi.org/10.1016/j.physc.2013.04.047
71. J. Hänisch, K. Iida, F. Kurth, et al., The effect of 45° grain boundaries and associated Fe particles on J_c and resistivity in $Ba(Fe_{0.9}Co_{0.1})_2As_2$ thin films. AIP Conf. Proc. **1574**, 260–267 (2014). https://doi.org/10.1063/1.4860633
72. E. Sarnelli, C. Nappi, C. Camerlingo, et al., Properties of Fe(Se,Te) bicrystal grain boundary junctions, SQUIDs, and nanostrips. IEEE Trans. Appl. Supercond. **27**(4), 7400104 (2017). https://doi.org/10.1109/TASC.2016.2636248
73. E. Sarnelli, M. Adamo, C. Nappi, et al., Properties of high-angle Fe(Se,Te) bicrystal grain boundary junctions. Appl. Phys. Lett. **104**(16), 162601 (2014). https://doi.org/10.1063/1.4871864
74. R. Gross, P. Chaudhari, D. Dimos, et al., Thermally activated phase slippage in high-T_c grain-boundary Josephson junctions. Phys. Rev. Lett. **64**(2), 228–231 (1990). https://doi.org/10.1103/PhysRevLett.64.228
75. Z.G. Ivanov, P.Å. Nilsson, D. Winkler, et al., Weak links and dc SQUIDS on artificial nonsymmetric grain boundaries in $YBa_2Cu_3O_{7-\delta}$. Appl. Phys. Lett. **59**(23), 3030 (1991). https://doi.org/10.1063/1.105783
76. B. Holzapfel, D. Verebelyi, C. Cantoni, et al., Low angle grain boundary transport properties of undoped and doped Y123 thin film bicrystals. Phys. C Supercond. Appl. **341**(348), 1431–1434 (2000). https://doi.org/10.1016/S0921-4534(00)00973-4

77. D.T. Verebelyi, C. Cantoni, J.D. Budai, et al., Critical current density of $YBa_2Cu_3O_{7-\delta}$ low-angle grain boundaries in self-field. Appl. Phys. Lett. **78**(14), 2031 (2001). https://doi.org/10.1063/1.1360230
78. N.F. Heinig, R.D. Redwing, J.E. Nordman, et al., Strong to weak coupling transition in low misorientation angle thin film $YBa_2Cu_3O_{7-x}$ bicrystals. Phys. Rev. B **60**(2), 1409 (1999). https://doi.org/10.1103/PhysRevB.60.1409
79. S.-W. Chan, Nature of grain boundaries as related to critical currents in superconducting $YBa_2Cu_3O_{7-x}$. J. Phys. Chem. Solids **55**(12), 1415–1432 (1994). https://doi.org/10.1016/0022-3697(94)90568-1
80. C.P. Poole, *Superconductivity*, 2nd edn. (Academic, Amsterdam, 2007)
81. G. Hammerl, A. Schmehl, R.R. Schulz, et al., Enhanced supercurrent density in polycrystalline $YBa_2Cu_3O_{7-d}$ at 77 K from calcium doping of grain boundaries. Nature **407**(6801), 162–164 (2000). https://doi.org/10.1038/35025014
82. P. Li, D. Abraimov, A. Polyanskii, et al., Study of grain boundary transparency in $(Yb_{1-x}Ca_x)Ba_2Cu_3O$ bicrystal thin films over a wide temperature, field, and field orientation range. Phys. Rev. B **91**(10), 104504 (2015). https://doi.org/10.1103/PhysRevB.91.104504
83. X. Song, G. Daniels, D.M. Feldmann, et al., Electromagnetic, atomic structure and chemistry changes induced by Ca-doping of low-angle $YBa_2Cu_3O_{7-d}$ grain boundaries. Nat. Mater. **4**(6), 470–475 (2005). https://doi.org/10.1038/nmat1394
84. E.F. Talantsev, W.P. Crump, Weak-links criterion for pnictide and cuprate superconductors. Supercond. Sci. Technol. **31**(12), 124001 (2018). https://doi.org/10.1088/1361-6668/aae50a
85. E.F. Talantsev, J.L. Tallon, Universal self-field critical current for thin-film superconductors. Nat. Commun. **6**, 7820 (2015). https://doi.org/10.1038/ncomms8820
86. V.J. Emery, S.A. Kivelson, Importance of phase fluctuations in superconductors with small superfluid density. Nature **374**(6521), 434 (1995). https://doi.org/10.1038/374434a0
87. S.-H. Hong, N.H. Lee, W.N. Kang, et al., Observation of weak coupling effects in $Ba_{0.6}K_{0.4}Fe_2As_2$ junctions patterned across a naturally formed grain boundary. Supercond. Sci. Technol. **27**(5), 055007 (2014). https://doi.org/10.1088/0953-2048/27/5/055007
88. S.-H. Hong, S.-G. Lee, S.-G. Jung, et al., Properties of FeSe nanobridges prepared by using a focused ion beam. J. Korean Phys. Soc. **61**(9), 1430–1434 (2012). https://doi.org/10.3938/jkps.61.1430
89. R. Schneider, A.G. Zaitsev, D. Fuchs, et al., Anisotropic grain-boundary effect on electronic transport in superconducting FeSe thin films. Supercond. Sci. Technol. **32**(2), 025001 (2019). https://doi.org/10.1088/1361-6668/aaf077
90. K. Iida, F. Kurth, M. Chihara, et al., Highly textured oxypnictide superconducting thin films on metal substrates. Appl. Phys. Lett. **105**(17), 172602 (2014). https://doi.org/10.1063/1.4900931
91. S. Haindl, M. Kidszun, A. Kauffmann, et al., High upper critical fields and evidence of weak-link behavior in superconducting $LaFeAsO_{1-x}F_x$ thin films. Phys. Rev. Lett. **104**(7), 077001 (2010). https://doi.org/10.1103/PhysRevLett.104.077001
92. S.-H. Hong, S.H. Lee, S.-G. Lee, et al., Fabrication of BaKFeAs intergrain nanobridges by using a focused ion beam. J. Korean Phys. Soc. **61**(9), 1449–1452 (2012). https://doi.org/10.3938/jkps.61.1449
93. K. Iida, J. Hänisch, S. Trommler, et al., Epitaxial growth of superconducting $Ba(Fe_{1-x}Co_x)_2As_2$ thin films on technical ion beam assisted deposition MgO substrates. Appl. Phys. Exp. **4**(1), 013103 (2011). https://doi.org/10.1143/APEX.4.013103
94. S. Trommler, J. Hänisch, V. Matias, et al., Architecture, microstructure and Jc anisotropy of highly oriented biaxially textured Co-doped $BaFe_2As_2$ on Fe/IBAD-MgO-buffered metal tapes. Supercond. Sci. Technol. **25**(8), 084019 (2012). https://doi.org/10.1088/0953-2048/25/8/084019
95. T. Katase, H. Hiramatsu, V. Matias, et al., Biaxially textured cobalt-doped $BaFe_2As_2$ films with high critical current density over 1 MA/cm^2 on MgO-buffered metal-tape flexible substrates. Appl. Phys. Lett. **98**(24), 242510 (2011). https://doi.org/10.1063/1.3599844

96. Z. Xu, P. Yuan, F. Fan, et al., Transport properties and pinning analysis for Co-doped $BaFe_2As_2$ thin films on metal tapes. Supercond. Sci. Technol. **31**(5), 055001 (2018). https://doi.org/10.1088/1361-6668/aab261
97. O. Rodríguez, A. Mariño, Voltage-current characteristics of epitaxial and misoriented $Ba(Fe_{1-x}Co_x)_2As_2$ thin films. Phys. C Supercond. Appl. **513**, 9–12 (2015). https://doi.org/10.1016/j.physc.2015.03.008
98. H. Sato, H. Hiramatsu, T. Kamiya, et al., Enhanced critical-current in P-doped $BaFe_2As_2$ thin films on metal substrates arising from poorly aligned grain boundaries. Sci. Rep. **6**, 36828 (2016). https://doi.org/10.1038/srep36828
99. K. Iida, H. Sato, C. Tarantini, et al., High-field transport properties of a P-doped $BaFe_2As_2$ film on technical substrate. Sci. Rep. **7**, 39951 (2017). https://doi.org/10.1038/srep39951
100. H. Hosono, K. Tanabe, E. Takayama-Muromachi, et al., Exploration of new superconductors and functional materials, and fabrication of superconducting tapes and wires of iron pnictides. Sci. Technol. Adv. Mater. **16**(3), 033503 (2015). https://doi.org/10.1088/1468-6996/16/3/033503
101. J. Huang, L. Chen, J. Jian, et al., A simplified superconducting coated conductor design with Fe-based superconductors on glass and flexible metallic substrates. J. Alloys Compd. **647**, 380–385 (2015). https://doi.org/10.1016/j.jallcom.2015.06.109
102. W. Si, J. Zhou, Q. Jie, et al., Iron-chalcogenide $FeSe_{0.5}Te_{0.5}$ coated superconducting tapes for high field applications. Appl. Phys. Lett. **98**(26), 262509 (2011). https://doi.org/10.1063/1.3606557
103. Z. Xu, P. Yuan, Y. Ma, et al., High-performance $FeSe_{0.5}Te_{0.5}$ thin films fabricated on less-well-textured flexible coated conductor templates. Supercond. Sci. Technol. **30**(3), 035003 (2017). https://doi.org/10.1088/1361-6668/30/3/035003
104. W. Si, S.J. Han, X. Shi, et al., High current superconductivity in $FeSe_{0.5}Te_{0.5}$-coated conductors at 30 tesla. Nat. Commun. **4**, 1397 (2013). https://doi.org/10.1038/ncomms2337
105. G. Sylva, A. Augieri, A. Mancini, et al., Fe(Se,Te) coated conductors deposited on simple RABiTS templates. Supercond. Sci. Technol. (2019) (accepted manuscript) https://doi.org/10.1088/1361-6668/ab0e98
106. M. Kidszun, S. Haindl, T. Thersleff, et al., Critical current scaling and anisotropy in oxypnictide superconductors. Phys. Rev. Lett. **106**(13), 137001 (2011). https://doi.org/10.1103/PhysRevLett.106.137001
107. G. Hammerl, A. Herrnberger, A. Schmehl, et al., Possible solution of the grain-boundary problem for applications of high-T_c superconductors. Appl. Phys. Lett. **81**(17), 3209–3211 (2002). https://doi.org/10.1063/1.1516831
108. J. Eickemeyer, D. Selbmann, R. Hühne, et al., Elongated grains in textured substrate tapes and their effect on transport currents in superconductor layers. Appl. Phys. Lett. **90**(1), 012510 (2007). https://doi.org/10.1063/1.2429905
109. C. Tarantini, K. Iida, J. Hänisch, et al., Intrinsic and extrinsic pinning in NdFeAs(O,F): vortex trapping and lock-in by the layered structure. Sci. Rep. **6**, 36047 (2016). https://doi.org/10.1038/srep36047
110. S. Demura, M. Tanaka, A. Yamashita, et al., Electrochemical deposition of FeSe on RABiTS tapes. J. Phys. Soc. Jpn. **85**(1), 015001 (2016). https://doi.org/10.7566/JPSJ.85.015001
111. A. Yamashita, R. Matsumoto, M. Tanaka, et al., Observation of zero resistance in as-electrodeposited FeSe. Solid State Commun. **270**, 72–75 (2018). https://doi.org/10.1016/j.ssc.2017.11.018